UNIVERSITY OF OKLAHOMA

GRADUATE COLLEGE

MOTOR THERMAL MODEL FOR AGING CONTROL APPLICATIONS

A THESIS

SUBMITTED TO THE GRADUATE FACULTY

in partial fulfillment of the requirements for the

Degree of

MASTER OF SCIENCE

By

CHIBUOKE ENEH
Norman, Oklahoma
2024

Downloaded from SHAREOK. Persistent Handle URL: https://hdl.handle.net/11244/341324

MOTOR THERMAL MODEL FOR AGING CONTROL APPLICATIONS

A THESIS APPROVED FOR THE
SCHOOL OF AEROSPACE AND MECHANICAL ENGINEERING

BY THE COMMITTEE CONSISTING OF

Dr. Dong Zhang, Chair

Dr. Jie Cai

Dr. Li Song

© Copyright by CHIBUOKE ENEH 2024
All Rights Reserved.

Dedicated

to my parents and siblings.

ACKNOWLEDGMENTS

I express my deepest gratitude to the special grace of God, which constantly guides me and strengthens me in my work. All of my accomplishments are dedicated to His glory.

I would like to acknowledge the financial support from DOE under award #DE-FOA-0002624.

A special acknowledgment is to my advisor, Dr. Cai, who invested many hours advising me on technical and professional aspects. His patience, understanding and commitment to high standards have shaped me into a better researcher. The lessons learned and experiences gained under Dr. Cai's mentorship are a timeless source of inspiration. The impact of this experience will benefit me throughout my career and life.

I am equally grateful to my esteemed committee members, Dr. Zhang and Dr. Song, and to my co-advisor, Dr. Moses, whose invaluable time and expertise contributed significantly to this endeavor. Their thoughtful engagement and discerning insights enriched the depth and quality of my work.

I am thankful to my flatmates, Ernesto, Jay and Shayaan for their moral support and encouragement throughout the research process.

Finally, my heartfelt gratitude go to my parents and siblings for their unconditional support and sacrifice through this journey.

TABLE OF CONTENTS

Acknowledgments v

List of Tables viii

List of Figures ix

Chapter 1: Introduction 1

1.1 Background on Motor Thermal Models 1

1.2 Motivation of This Study 2

Chapter 2: Literature review 4

2.1 Gap and New Contributions of This Study 9

Chapter 3: Motor Thermal Model 10

3.1 Motor General Description 10

3.1.1 Motor Cooling System 11

3.2 Motor Thermal Model 12

3.2.1 Motor Thermal Circuit Capacitance and Resistance 13

3.2.2 Lumped Parameter Thermal Network Model 16

3.3 Test Motor Specifications 20

Chapter 4: Thermal Model Validation 22

4.1 Motor Testing Rig 22

4.1.1 Motor Loading Mechanism 23

4.2 Temperature Measurement Instrumentation 24

4.3 Temperature-Controlled Enclosure for Induction Motor 26

4.4 Thermal Model Parameter Tuning 26

4.4.1 Test Results 27

4.4.2 Individually Tuned Motor Thermal Model Validation Results 34

4.5 Generic Motor Thermal Model Development 41

4.5.1 Generic Motor Thermal Model Tuning Results 44

Chapter 5: Frequency Regulation Test Results 51

5.1 Motor Performance Curves 52

5.2 Modulation Test Results 55

5.3 Baseline Test Results 58

5.4 Motor Thermal Model Results 60

Chapter 6: Conclusions 63

6.1 Future Work 63

References 65

LIST OF TABLES

3.1 Material coefficients for motor thermal capacitance and conductive resistance 15

3.2 Material coefficients for motor thermal convective resistance 16

3.3 Induction motor main specifications 21

4.1 Test matrix for induction motor 27

4.2 Calibrated material parameters for motor thermal capacitance and resistance 35

4.3 Calibrated heat transfer coefficients for motor components at different speeds 36

LIST OF FIGURES

3.1 Airflow path representation. Grey arrows indicate the rotation of the shaft, blue arrows indicate airflow path. 12

3.2 Heat flow through the induction motor cross section 17

3.3 Thermal network model used in this study 18

3.4 Case study induction motor 21

4.1 Prototype motor with experimental set up 23

4.2 Thermograms showing the hot spots within the stator winding for thermocouple placement 25

4.3 Temperature distribution for 50% speed and half load 28

4.4 Temperature distribution for 50% speed and full load 29

4.5 Temperature distribution for 75% speed and half load 30

4.6 Temperature distribution for 75% speed and full load 31

4.7 Temperature distribution for 100% speed and half load 32

4.8 Temperature distribution for 100% speed and full load 33

4.9 Simulation and test thermal profile for 50% speed and half load 37

4.10 Simulation and test thermal profile for 50% speed and full load 38

4.11 Simulation and test thermal profile for 75% speed and half load 39

4.12 Simulation and test thermal profile for 75% speed and full load 40

4.13 Simulation and test thermal profile for 100% speed and half load 40

4.14 Simulation and test thermal profile for 100% speed and full load 41

4.15 Correlation between end-winding heat transfer coefficient and motor speed . 42

4.16 Correlation between motor casing heat transfer coefficient and motor speed 43

4.17 Generic model simulation and test thermal profile for 50% speed and half load 45

4.18 Generic model simulation and test thermal profile for 50% speed and full load 46

4.19 Generic model simulation and test thermal profile for 75% speed and half load 47

4.20 Generic model simulation and test thermal profile for 75% speed and full load 48

4.21 Generic model simulation and test thermal profile for 100% speed and half load 49

4.22 Generic model simulation and test thermal profile for 100% speed and full load 49

5.1 Speed vs. Power curve 53

5.2 Speed vs. Torque curve 54

5.3 Torque vs. Frequency difference curve 55

5.4 Power comparison between signal target and motor result 56

5.5 Torque comparison between signal target and motor result 57

5.6 Temperature distribution of induction motor for the modulation test 58

5.7 Speed vs. Airflow curve 59

5.8 Temperature distribution of induction motor for the baseline test 60

5.9 Motor simulation and experimental thermal results comparison for the modulation test 61

5.10 Motor simulation and experimental thermal results comparison for the baseline test 62

ABSTRACT

Deeper integration of renewable energy sources on the electric grid has increased flexibility requirements across power systems, from generation to transmission/distribution and consumer equipment. On the consumer end, the use of variable-speed electric motors in commercial and residential heating, ventilation, and air-conditioning (HVAC) applications is becoming widespread due to their energy and cost-saving benefits compared to single-speed motors. However, the enhanced features and operational flexibility of these modern motors may come at the cost of increased thermal stress on the motor components, particularly the stator winding insulation. To address this challenge, this thesis presents the development of a generic Lumped Parameter Thermal Network (LPTN) model that can accurately capture the thermal behavior of induction motors under dynamic and varying speed and load conditions. The LPTN model parameters are systematically tuned and calibrated using test data from laboratory tests covering different speed and load settings, achieving a maximum error of 4.8°C between the model predictions and experimental measurements for a 3 HP test motor. The dynamic, modulating control of the motor leads to winding temperatures 7.3°C higher than that under constant-speed control, showing significant aging effect of dynamic operation of motors due to flexibility provision. The calibrated thermal model and the physical 3 HP motor are tested under constant and modulation speed control cases. The thermal model is able to predict the hot spot temperature difference between these test two cases for the test motor with an accuracy of 0.2°C, validating the model's capability to accurately replicate the change in the thermal behavior of the case study motor. This generic, calibrated LPTN model can serve as a powerful tool to facilitate faster and more cost-effective development of control strategies and maintenance plans for variable-speed electric motors, ultimately improving their reliability and energy efficiency in a wide range of commercial and residential applications.

CHAPTER 1

INTRODUCTION

Electric motors play a significant role in the energy industry worldwide, accounting for more than 40% of global energy consumption [1]. Motors are also one of the core components of many energy systems working with electricity, and are widely used in the energy conversion industry. A large portion of the motor electricity consumption can be attributed to mid-size motors with output powers ranging from 0.75 kW to 375 kW. These comprise 68% of the combined total of all electromagnetic motors and consume more electricity than the motors in other size categories [2]. Motors used in heating, ventilation and air-conditioning (HVAC) systems fall under this category and they consume approximately 31% of residential end-delivered energy in the U.S. [3]. Manufacturers typically provide compressor motors with a rated lifetime of 10 years for the U.S. market [4]; however, these motors are predominantly driven at constant, nominal speed. The recent introduction of variable-speed HVAC units to the market, however, demands a revisit of this lifetime assessment, especially under dynamic operating conditions.

1.1 Background on Motor Thermal Models

Motor thermal performance characterization has become an important area of research due to the evolving operational requirements of electric motors. Over the years, significant advancements have been made in the design and performance of electric motors, resulting in improved performances such as higher efficiency, accurate control, operation above nominal

speed, and increased power density. However, these enhanced capabilities have come at the cost of increased thermal stress on the motor components. One major issue that has arisen is the degradation of the stator winding insulation due to the elevated temperatures within the motor [5]. As motors operate at higher power densities and speeds, the thermal loading on the system increases, leading to accelerated wear and potential failure of the insulation. This has prompted extensive research efforts focused on developing accurate thermal models that can characterize the motor's thermal behavior. By accurately predicting the temperature distribution and hot spots within the motor, these thermal models enable engineers to design more robust thermal management strategies, implement better control algorithms, and optimize maintenance schedules. The availability of reliable thermal models has facilitated faster and more cost-effective development of high-performance, reliable electric motor systems.

1.2 Motivation of This Study

The fast growth in electrical demand leads to increasing importance of demand response, where load is to be shifted from peak demand hours in the middle of the day to off-peak hours at night, resulting in energy cost savings and increased system-level efficiency. However, the increasing integration of renewable energy sources on the electric grid and the inherent unreliability of renewable resources has necessitated the availability of rapid response resources, such as diesel and natural gas generators, to ensure constant fulfillment of load during low-renewable times. These fluctuations in supply and demand have made it imperative to employ flexibility resources across all sectors of the power grid, from generation to transmission/distribution and consumers.

On the consumer end, the use of variable-speed electric motors in commercial and resi-

dential equipment fosters this required flexibility. Variable-speed motors are preferred over single-speed motors as they can provide the same level of service while operating at half-speed and consuming only 25% of the power required by the latter under certain operating conditions [6]. Additionally, variable-speed motors exhibit a fast response to flexibility requests, which make them suitable for fast balancing services like frequency regulation. The long-term energy and cost savings provided by these flexible energy conversion systems have incentivized research to study the impact of variable-speed operation on the material reliability of motor components.

CHAPTER 2

LITERATURE REVIEW

Thermal modeling of electric motors has become prevalent over the years because it simplifies the thermal analysis of these complex systems and aids characterization of their aging behavior as a result of the induced thermal stress. Assessing the insulation material integrity is the main goal of the thermal analysis effort because stator winding insulation breakdown is one of the major sources of squirrel-cage motor failures [7, 8]. According to [9], the degradation of stator winding insulation and its ultimate breakdown is influenced by four factors that act simultaneously on the dielectric: thermal aging of the insulation; voltage surges caused by lightning, switching, or recurrent pulses; insulation chaffing and shearing caused by mechanical stress due to vibrations and shearing forces; and chemical deterioration due to environmental factors such as aggressive chemicals or hydrocarbons. When the motor ramps up and down continuously under dynamic load conditions, the mechanical and thermal stresses on the insulation become heightened, which is common for variable frequency drive-fed electric motors. Hence, developing digital twins of these electric motors is essential to thoroughly characterize the resulting aging effect [10].

Different types of thermal modeling techniques have been proposed and they each have their own advantages based on the mode of heat transfer under study, required computational complexity, and accuracy of simulation results [11, 12]. From the mathematical point of view, thermal modeling techniques are categorized into three main classes as follows [13]:

- Analytical;
- Semi-analytical; and

- Numerical.

Analytical methods, as their name suggests, rely on closed-form solutions of fundamental heat equations. They typically offer a computing speed advantage over numerical methods but are limited to simple geometries where such solutions are available. Numerical methods, on the other hand, solve differential heat equations by dividing the motor's geometry into multiple smaller sections through meshing. Accurate meshing and boundary condition settings are crucial for reliable results. Additionally, numerical methods require iterative calculations, which is a primary reason for their high computational demand. When using numerical methods, factors like consistency, stability, convergence, and accuracy need careful consideration. For energy systems with mainly solid parts that have limited interaction with fluid media, finite element analysis (FEA) is the best numerical modeling approach to employ since this has a high accuracy for conduction analysis, although the computational burden of calculations is a limiting factor due to the large number of meshes [14]. On the other hand, computational fluid dynamics (CFD) is the preferred numerical method for the simulation of systems involving fluids, due to its high accuracy in convection analysis, which is the dominant heat transfer mechanism within fluids and between solid surfaces and fluids. This two-phase computational capability in CFD makes it more flexible than FEA [15, 16], and an important tool in the thermal analysis and cooling system design of electric motors. The two numerical methods mentioned so far require the development of a high-fidelity three-dimensional digital twin of the electric motor to obtain accurate results, and their computational demand is quite high due to the large number of meshes involved.

While models with higher accuracy are useful in design stages, models with low computational burden are needed for practical, real-time applications such as thermal monitoring [17]. Lumped parameter thermal networks (LPTN) offer fast computing speed and a relatively high prediction accuracy. They have remained relevant for years due to this advantage. In this approach, the components with similar temperatures are lumped together

and treated as a node [18]. Depending on the required accuracy and computational complexity, LPTNs can be implemented with various assumptions. For example, the effect of radiation or some power losses such as friction can be neglected in electric motor applications [17]. When developing an LPTN for thermal modeling of electric motors, an analogy can be drawn between electrical and thermal circuits shown in the equations in Chapter 3. Two distinct modes of operation need to be considered when employing this modeling approach: stationary and non-stationary. In the stationary mode, the thermal capacitors can be neglected, as the system is assumed to have reached a steady-state condition. Conversely, for the non-stationary mode, the thermal capacitors are necessary to accurately capture the transient thermal behavior. The LPTN is constructed by lumping together similar temperature points and designating them as nodes within the network. These nodes are then connected by thermal resistors, which represent the conduction and convection mechanisms within the system [18].

Combining LPTNs with other thermal modeling techniques and optimal parameter estimation methods have been proposed for improving the accuracy of the models [19]. The estimation of certain parameters, such as those related to the manufacturing process or the machine operating conditions, has proven to be a challenging task. Some expressions for the estimation of the heat transfer coefficients and thermal resistances have been derived in [17], which require knowledge of the machine geometry and the utilized materials. In [20], the thermal parameters of an LPTN for a permanent magnet synchronous machine (PMSM) were determined using two offline tests: the DC current test and the no-load rotational test. This study focused on the determination of interface thermal resistances and the convection heat transfer coefficients required for the LPTN. Gauss-Newton, Levenberg-Marquardt, and least square algorithms have been employed in [19] to identify ten thermal parameters, including four convective heat transfer coefficients in different regions, four contact conductance between the regions, conductivity in winding, and thermal resistance of the ball-bearing.

A calibration technique for a generic thermal model of electrical machines has been proposed in [21]. This approach is based on the combination of two experimental tests: a short-duty transient excitation for extraction of winding thermal capacitances, and a steady-state excitation to estimate thermal resistances related to the heat transfer from the winding. To enhance the accuracy of parameter estimation, an approach based on the coupling of analytical and local numerical methods has been proposed in [22] for forced air-cooled motors. In this approach, the winding conduction thermal resistance is derived from 2-D numerical calculations, while the convection resistance of the airflow in the end region is obtained from 3-D local numerical analysis. The boundary conditions are derived from a combination of the results of the numerical analysis and LPTN. An analytical approach for accurate calculation of the heat transfer coefficients, including convection coefficient in natural and forced convection modes, radiation coefficients, and Nusselt number has been proposed in [23]. Measured and empirical data have been used in [24] for modeling losses in a PMSM, in which an LPTN with 4 nodes has been considered.

Due to the possible variation of thermal parameters, such as heat transfer coefficients, during operation under dynamic conditions, LPTNs cannot be considered as time-invariant linear models. To deal with this non-linear behavior they can be modeled as linear parameter varying models [25]. Generally, three categories of methods are utilized for modeling and identification of linear parameter varying models [26] - glocal, local and global. Three glocal methods have been suggested in [25] for PMSMs. Besides, a global method for parameter identification in LPTNs has been considered in [27]. The advantage of this approach is its ability to avoid convergence to suboptimal local minima.

Power losses, heat transfer coefficients, and thermal capacitances are temperature-dependent parameters. To account for this dependence, an extended version of LPTNs has been developed in [28]. This extended approach incorporates the effect of temperature into the heat equations, which leads to a decrease in simulation time and enables faster analysis of the

thermal behavior of the machine. The impact of insulation aging on the thermal performance of electrical machines has been investigated in [29], where an extended version of LPTNs with the ability to incorporate thermal variations related to insulation aging has been proposed. Additionally, an analytical method applying the T-sum rule on the LPTNs has been presented in [21]. This approach converts the differential equations into pure matrix calculations, which makes it suitable for real-time applications. This method achieves better computational performance while maintaining similar accuracy. Furthermore, a 3D LPTN for the transient thermal study of an axial flux PMSM has been proposed in [30]. This LPTN can account for the cooling provided by the air inside the channel between the permanent magnets on the motor's disks. Further investigation of the impact of geometrical parameters on the temperature of the different parts of the machine using this LPTN has been carried out in [31].

These studies show that a precise electric motor numerical model can be developed by training a lumped parameter thermal network (LPTN) with appropriate experimental data. Further, they suggest improving the performance of the thermal model through accurate parameter estimation methods. They also highlight the impact of insulation aging on the thermal behavior of electrical machines. However, these investigations were done for constant speed and load conditions. This thesis reports the development of a generic motor thermal model that captures the impact of running an electric motor under variable speed and load conditions on its thermal dynamics by: (1) tuning/calibrating the thermal model with test data from laboratory test results covering different operating conditions; (2) testing both the case study motor and the calibrated thermal model under constant and modulating speed cases; and (3) comparing the temperature difference between the test motor and thermal model thermal profiles.

2.1 Gap and New Contributions of This Study

Electric motors with dynamic load response capabilities have found widespread acceptance, especially among consumers due to their energy saving benefits and potential for grid reliability support. However, the impact of flexibility provision on the lifespan of electric motors remains obscure, and this poses a major setback to the technology acceptance among equipment manufacturers, system operators and business investors.

This work fills this knowledge gap by:

1. Conducting laboratory experiments to gather empirical data on impacts of variable-speed operation on the lifetime of electric motors;
2. Developing a calibrated numerical model to characterize motor aging behavior and estimate the lifetime impact under dynamic operating conditions.

The results of this study provide a solid background for aging-aware control measures to be developed and applied on electric motors, thus improving their performance under variable speed and load conditions and increasing flexibility that can be provided by motorized storage systems.

CHAPTER 3

MOTOR THERMAL MODEL

Thermal analysis of winding insulation is a vital step for the productive design of electrical motors. It proves even more useful in the maintenance of these machines, making it possible for engineers to monitor and optimize the performance of motors through better thermal management. Experts utilize thermal models to predict the thermal behavior of the prototype and to ensure that it has a satisfactory performance under various operating conditions.

3.1 Motor General Description

This section describes the physical and electro-mechanical features of generic induction motors. The shaft is mounted on a squirrel-cage rotor with laminated windings filling the hollow cage. This is the only mobile part of the motor and is functionally the most important component in the machine. The stator encompasses this rotor and provides the magnetic energy needed to power the rotor, causing it to rotate. This stator is split into a main core which is made of solid steel, and slots on the inner circumference where laminated copper windings are packed. The overall stator winding is also divided into slot and end-windings based on whether it is located along the slot grooves, or at the open end of the stator core, respectively. This entire system is housed by the motor round frame which simultaneously provides protection for the energy conversion device and safety for operators. Mounting bases are attached to this round casing, enabling easy handling and installation.

3.1.1 Motor Cooling System

The National Electrical Manufacturers Association (NEMA) classifies motor enclosures into two categories - open machines and totally enclosed machines. Motors in the first category are self ventilated and usually have internal fans that assist air circulation within the motor. They are typically intended for use in indoor spaces where the environment is clean. The second group of motors are, as their name implies, totally enclosed and depend on external air ventilation for cooling. This type of motors are suitable for harsh outdoor and hazardous environments. The cooling system for the motor of interest in this study is self ventilated (open drip proof type). This poses a challenge for the modeling engineer for a number of reasons. Firstly, air is continuously exchanged between the interior parts of the motor and the ambient. While this is more thermally efficient for the motor unlike the totally enclosed fan-cooled (TEFC) types, it is complicated to design a model that accurately captures the thermal stratification that occur in the motor interior. Secondly, the heat transfer coefficients are calculated based on correlations which need motor speed input since the airflow in proximity with the exchanging surfaces will vary according to the operating speed of the motor. Figure 3.1 illustrates the airflow path in the interior of the motor. Air goes in from the openings at the front plate and circular casing, flows through the air gap propelled by the rotation of the shaft and leaves from the back end plate.

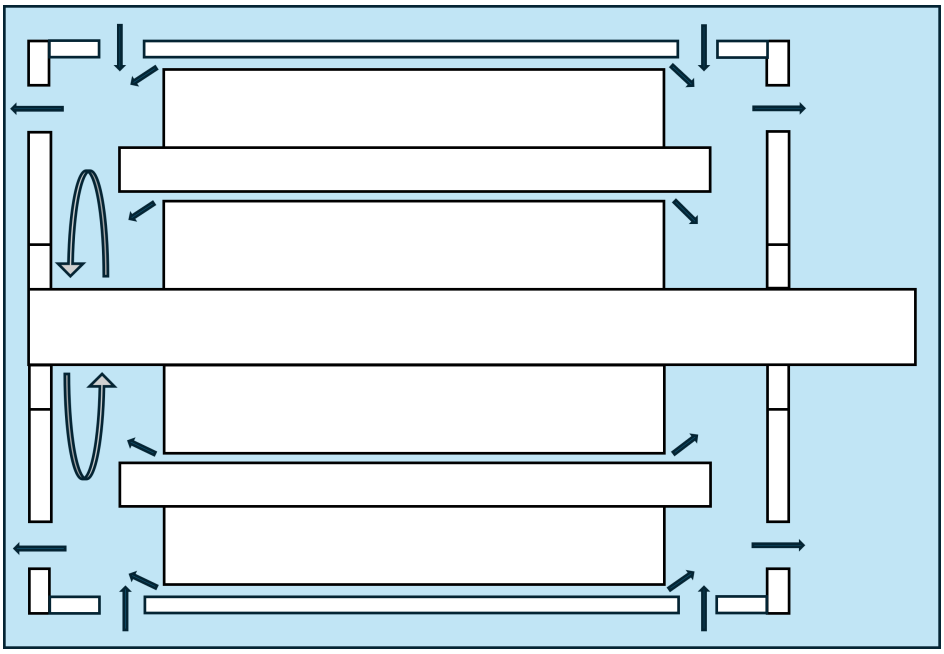

Figure 3.1: Airflow path representation. Grey arrows indicate the rotation of the shaft, blue arrows indicate airflow path.

3.2 Motor Thermal Model

In this section, the development of the dynamic thermal motor model used for thermal behavior analysis and control testing is discussed. There are many types of thermal model representations used to analyze the thermal dynamics in energy conversion systems. Some of them are mentioned as follows:

1. Sub-domain models (complex)
2. Lumped parameter thermal networks (fast)
3. Finite element models (high accuracy for conduction)
4. Computational fluid dynamics (high accuracy for convection)
5. Coupled analysis (multi-domain models)

6. Reduced order models

7. Hybrid thermal models (combination of 2 or more thermal models)

A lumped parameter thermal network (LPTN) model uses a thermal circuit to capture the motor dynamics. The LPTN approach is chosen over the finite element analysis (FEA) method because it has the advantage of being less computationally expensive by compartmentalizing components with similar temperature into single nodes while also maintaining a good level of accuracy in temperature profile prediction.

Due to the loss of geometric precision in employing the LPTN approach over the FEA method, the thermal circuit is extended as much as possible to accurately represent the axial and radial heat flow paths from the center of the shaft to the ambient around the motor end plates and round casing. This model also captures the influence of ambient air mixing with internal air within the motor due to the ODP enclosure type. A high-fidelity LPTN model is developed by [32] which initially had 78 nodes before being reduced to a final version with 24 nodes. This nodal reduction led to a 77% decrease in computational time with a temperature difference of 3°C in accuracy. The adaptive LPTN thermal model in this study is developed following the steps in this reference.

3.2.1 Motor Thermal Circuit Capacitance and Resistance

Thermal capacitances and resistances of the motor parts are determined by considering the geometry and material of the specific part. The assumption that the material is homogeneous and has same properties in every part of the motor is made to simplify the calculation. Thermal mass which is represented by the capacitance, is easily calculated as the product of

density (ρ), volume (V) and specific heat (c) as can be seen in Equation 3.1.

$$C = \rho V c \tag{3.1}$$

The density of the solid parts is also assumed constant to make things less complicated. However, density increases with heat in reality. Generally, all material properties are temperature dependent, especially after long exposure to high heat levels which the simulation thermal range will not typically get to. Hence, these properties are reasonably assumed constant for the model developed in this study.

Estimation of the thermal resistances is more complicated due to the different complex geometrical configurations of the motor parts. The cylindrical shaft, parallelepiped rotor bars and stator slots, and axial thermal resistance connections are the simple elements that can easily be determined by equations in the form:

$$R_{conduction} = \frac{\Delta x}{kA}, \tag{3.2}$$

$$R_{convection} = \frac{1}{hA} \tag{3.3}$$

Δx is the thickness of the solid body, k is the material conductivity, A is the area perpendicular to heat flow, and h is the heat transfer coefficient. For more complicated elements like the hollow-cylindrical stator core and rotor duct, their radial and axial directions have to be considered when applying Equation 3.4 since the cross-sectional area varies along the radius logarithmically.

$$R = \frac{ln\frac{r_o}{r_i}}{k2\pi l} \tag{3.4}$$

The packed conductors within the stator slot is considered a trapezoid with the resistance

expressed as:

$$R = y\frac{ln\frac{x_o}{x_i}}{k(x_o - x_i)l} \tag{3.5}$$

where y and l are the height and length of the trapezoidal element, respectively, x_o and x_i are the outer and inner widths of the element. The slot fill factor of an induction motor, which is the ratio of the cross-sectional area of copper wire in a stator slot to the total available space in the slot, ranges between 0.4 to 0.6, hence, the overall winding resistance is multiplied by the fill factor to determine the effective thermal resistance for the copper winding [33]. The list of parameters of the different components used to determine the thermal capacitance and resistance is shown in Table 3.1 below.

Component	**Parameter**		
	Specific heat c **(J/kgK)**	**Density** ρ **(kg/m^3)**	**Conductivity** k **(W/mK)**
rotor	460	7650	28
winding	385	8933	401
insulation	1700	1400	0.2
stator	460	7650	28
casing	833	2790	168

Table 3.1: Material coefficients for motor thermal capacitance and conductive resistance

Table 3.3, 3.5 and 3.9 of [32]

Table 3.2 presents the list of parameters of the different components used to determine the conductive thermal resistance.

Parameter	Description	Value	Unit
Heat transfer coefficient h	rotor	25	W/mK
	slot winding	25	W/mK
	end-winding	variable	W/mK
	stator	37	W/mK
	casing	variable	W/mK

Table 3.2: Material coefficients for motor thermal convective resistance

3.2.2 Lumped Parameter Thermal Network Model

Figure 3.2 shows the longitudinal cross section of the induction motor and demonstrates the heat transfer paths across the motor components from the middle of the shaft to the surrounding air. Since the geometry of the motor is symmetrical, the heat flow direction is presented for only a half of the cross section. The thermal circuit network is developed based on these heat transfer paths by connecting nodes that represent each numbered motor component together using either conductive or convective resistances, or both in parallel. Capacitances are connected to these nodes as well signifying their associated thermal mass. Properly calibrated LPTN models aid fast simulation with almost same degree of accuracy as high-fidelity FEA or computational fluid dynamics (CFD) models developed in reference materials.

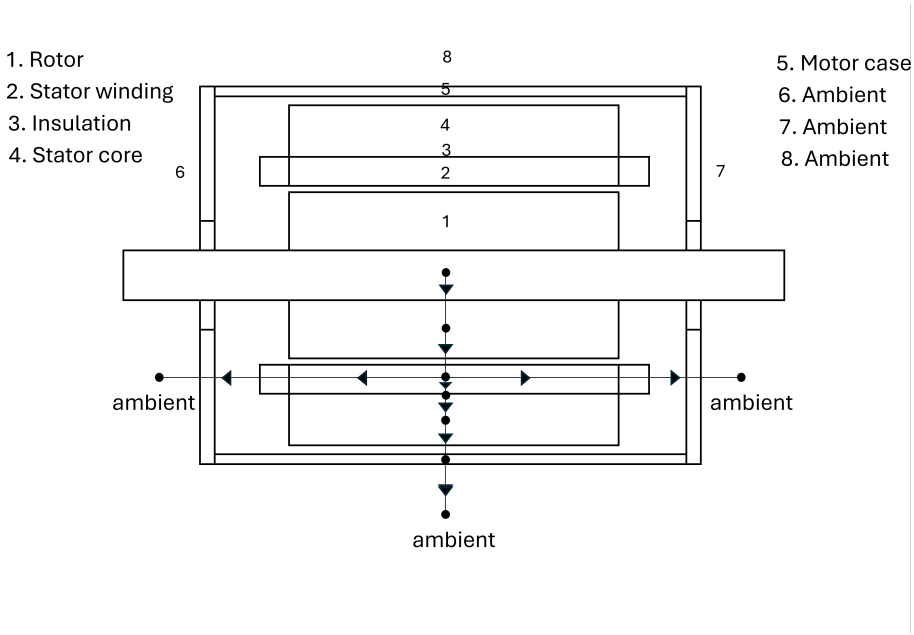

Figure 3.2: Heat flow through the induction motor cross section

The thermal circuit model showing the resistances and capacitances can be seen in Figure 3.3. This circuit is developed in MATLAB SimScape environment, and has one main tree representing the radial heat flow from the rotor bars through the air gap to the stator winding and then to the stator core before reaching the ambient through the round casing via convection. The other two branches represent the axial heat flow path to the end-plate air through the stator end-windings by convection. The model consists of 9 nodes and 8 thermal resistances. In the model, the stator of the induction motor has networks for the stator core and the stator winding. The end-windings do not have a specified node, but their influence is reflected by the axially connected resistances that end in the ambient-temperature nodes 6 and 7. Heat transfer from the rotor through the air gap is assumed to go directly to the stator winding with negligible impact on the stator teeth. By connecting the rotor, stator, frame, and ambient networks through thermal resistances, the thermal network model for the induction motor is realized. The SimScape solver configuration consists of a fixed-step *auto* solver with a sample time of 2 seconds. This *auto* selection implies that SimScape will select the appropriate solver to run the physics-based simulation depending on the requirements of

the developed model.

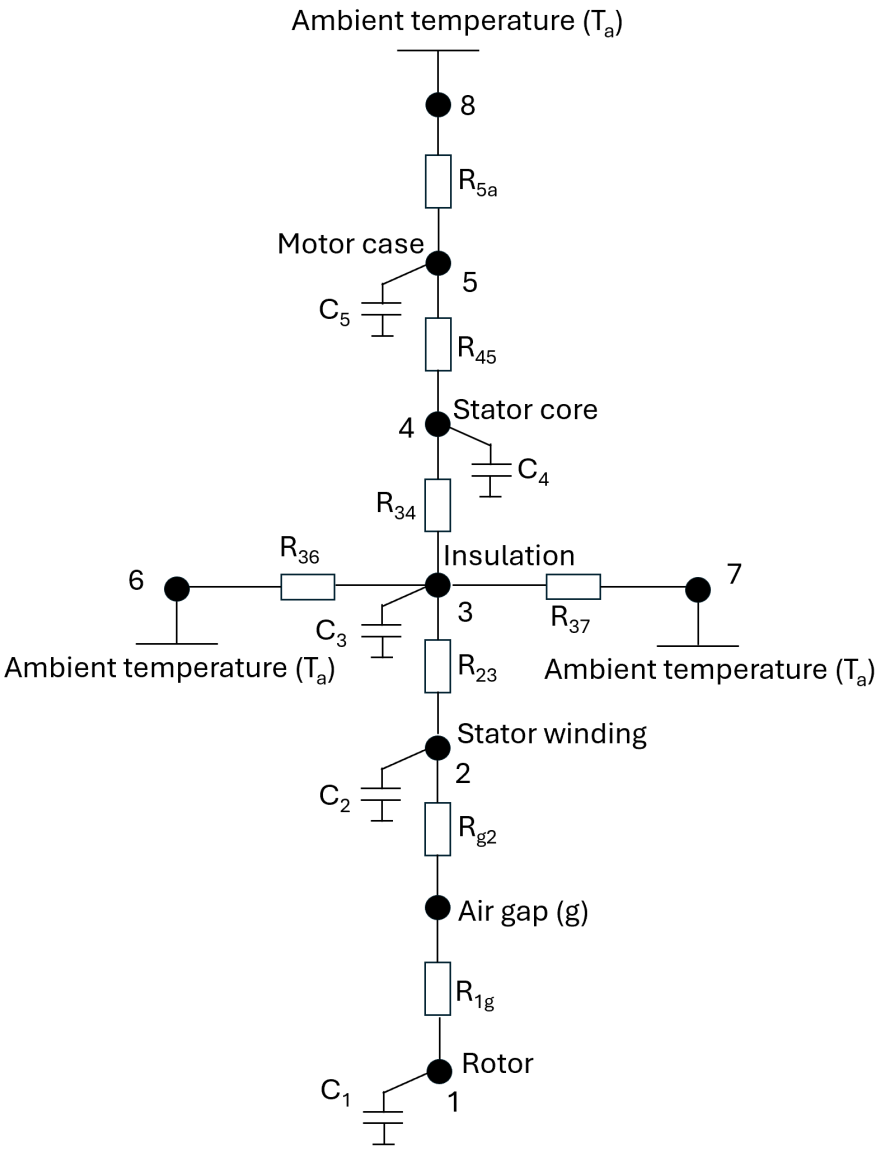

Figure 3.3: Thermal network model used in this study

The heat sources for this model are the power losses generated in the motor which are predominantly the stator copper losses and the stator core losses. Copper losses are generated in the stator winding (node 2 in Figure 3.3), and are mathematically represented as a product of the winding resistance and the supply current. These losses are caused by supply voltage imbalance and harmonics. Core or iron losses on the other hand are a representation

of power loss in the stator material (node 4). They are a combination of hysteresis losses, eddy current losses and excess losses in the stator core [34]. Other losses such as the rotor bar losses and mechanical losses due to bearing friction are not as significant as the first two, hence, they are neglected for this study.

Mathematically, this thermal network model is described in state space form representing the energy balance equations for all temperature nodes. Solving the thermal network involves finding the solution to the governing ordinary differential equations. SimScape solver uses the information from the developed network model to create a numerical linear system of the form shown in Equation 3.6. It is clear that the dimension of the matrix system depends on the number of temperature nodes in the thermal circuit. Each node is considered a lumped system, which has a control volume with a boundary that defines the heat entering the system or leaving it, and the generated heat within the system. The temperature is assumed to be uniform in each lumped node.

$$\begin{bmatrix} \frac{dT_1}{dt} \\ \frac{dT_2}{dt} \\ \frac{dT_3}{dt} \\ \frac{dT_4}{dt} \\ \frac{dT_5}{dt} \end{bmatrix} = \begin{bmatrix} \frac{1}{C_1} & 0 & 0 & 0 & 0 & 0 \\ 0 & \frac{1}{C_2} & 0 & 0 & 0 & 0 \\ 0 & 0 & \frac{1}{C_3} & 0 & 0 & \frac{G_{36}+G_{37}}{C_3} \\ 0 & 0 & 0 & \frac{1}{C_4} & 0 & 0 \\ 0 & 0 & 0 & 0 & \frac{1}{C_5} & \frac{G_{5a}}{C_5} \end{bmatrix} \begin{bmatrix} P_1 \\ P_2 \\ P_3 \\ P_4 \\ P_5 \\ T_a \end{bmatrix} \tag{3.6}$$

$$- \begin{bmatrix} \frac{-(G_{1g}+G_{g2})}{C_1} & \frac{G_{1g}+G_{g2}}{C_1} & 0 & 0 & 0 \\ \frac{G_{1g}+G_{g2}}{C_2} & \frac{-(G_{1g}+G_{g2}+G_{23})}{C_2} & \frac{G_{23}}{C_2} & 0 & 0 \\ 0 & \frac{G_{23}}{C_3} & \frac{-(G_{23}+G_{34}+G_{36}+G_{37})}{C_3} & \frac{G_{34}}{C_3} & 0 \\ 0 & 0 & \frac{G_{34}}{C_4} & \frac{-(G_{34}+G_{45})}{C_4} & \frac{G_{45}}{C_4} \\ 0 & 0 & 0 & \frac{G_{45}}{C_5} & \frac{-(G_{45}+G_{5a})}{C_5} \end{bmatrix} \begin{bmatrix} T_1 \\ T_2 \\ T_3 \\ T_4 \\ T_5 \end{bmatrix} \tag{3.7}$$

T_a represents the ambient temperature nodes 6, 7 and 8. The term G_{ij} describes the thermal conductance, which is mathematically the inverse of the thermal resistance. The thermal conductances around the air gap node are merged. The heat source term P_i is set to zero for nodes where no heat generation is considered. The transfer of heat through these nodes is based only on the temperature difference between the specific node and the neighboring nodes.

3.3 Test Motor Specifications

The test motor considered in the experimental setup can be seen in Figure 3.4. It is an induction machine designed for HVAC pump or fan applications. The motor is a 4-pole induction machine, the rotor type is squirrel cage with casted aluminum, stator and rotor are laminated. Technical specifications are summarized in Table 3.3.



Figure 3.4: Case study induction motor

Motor Parameter	**Value**
Voltage	230 V
Current	7.94 A
Power	2.2 kW/ 3 HP
PF (cos ϕ)	0.80
Speed	1735 RPM
Frequency	60 Hz
Poles	4

Table 3.3: Induction motor main specifications

CHAPTER 4

THERMAL MODEL VALIDATION

This chapter discusses the instrumentation and measurement system put in place to carry out tests on the motor at the laboratory and how these test results are used to calibrate and validate the motor numerical thermal model. The experimental results of the fully developed thermal model are also shown and compared with the experimental data for analysis.

4.1 Motor Testing Rig

The motor testing and loading rig shown in Figure 4.1 encompasses the complete experimental set up for running, loading, monitoring, collecting and recording the mechanical and electrical operation data of the motor. Two programmable logic controllers (PLCs) are employed for automation in this set-up.

The thermal and mechanical results are recorded by the *Siemens SIMATIC 7-1200 1215C PLC*. This PLC is connected with two thermocouple modules, each having 8 channels for temperature measurements, and an analog input module with 8 channels for motor torque output readings. The actual torque measurement is done by the *ATO Digital Rotary Torque Sensor*, which has a pulse signal output that the Siemens PLC can detect. This torque sensor is placed between the driving induction motor and the loading dynamometer for effective data collection. The electrical results are handled by the *National Instruments CRIO controller* which collects voltage, current, power, and harmonics distortion readings. Power analyzers and other sensors for electrical measurements are located at the case study motor

VFD outlet to effectively capture the power input to the test motor, harmonics and other necessary electrical data.

The STEP 7 Professional V17 software package that includes TIA Portal and WinCC is used to program the measurement and testing control logics and the user interface. The results collected by the Siemens CPU (Slave 1) and the CRIO controller (Slave 2) are sent to the control computer (Master) via MODBUS where all the test results are collected and stored.

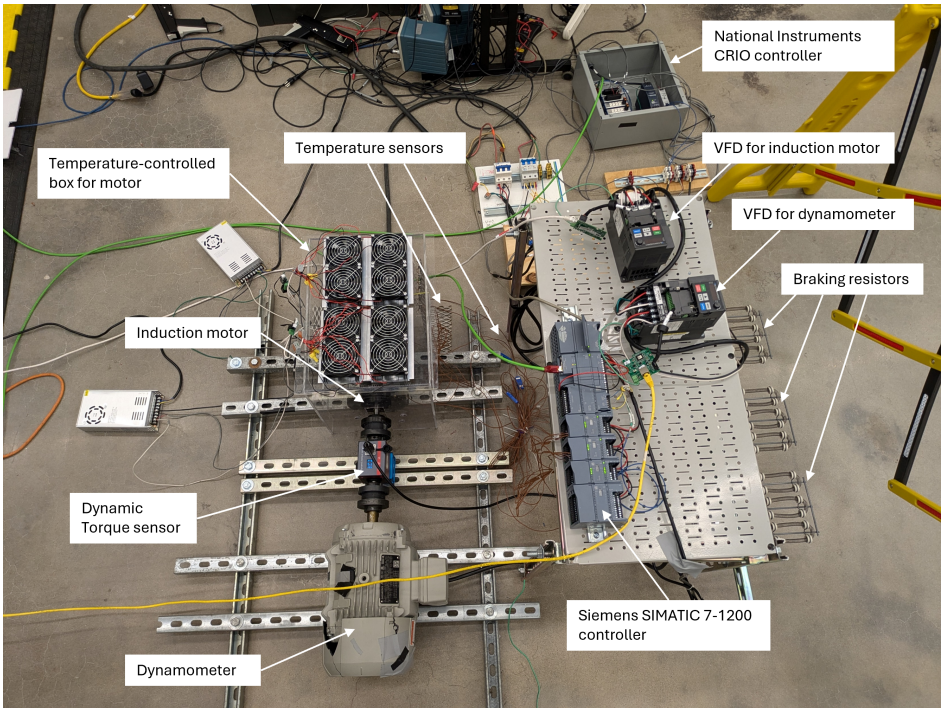

Figure 4.1: Prototype motor with experimental set up

4.1.1 Motor Loading Mechanism

The case study motor is tested under different speed and load conditions for this study. The motor test rig comprises a pair of three-phase induction machines powered by variable frequency drives (VFDs). One of the induction machines is the case study motor, while the

other functions as the dynamometer that provides the load. The speed setting for the test motor is achieved by adjusting the frequency of its supply VFD accordingly, while the load setting is achieved by operating the dynamometer supply VFD in dynamic braking mode with braking resistors to provide the necessary load to the test motor. The dynamometer induction motor is subjected to dynamic braking by its VFD to replicate real-world loading scenarios on the case study induction motor.

To activate dynamic braking, the supply frequency of the test motor is specified (60 Hz for rated conditions), while the dynamometer operational frequency is kept below this value. Supplying a lower frequency to the dynamometer than the test motor results in a slower rotating magnetic field in the dyno than that of the test motor. This causes the rotor to rotate faster than the synchronous speed of the stator magnetic field, effectively making it function as a generator and inducing a current in the stator windings. As the frequency difference between the test motor and the dynamometer increases, stronger induction occurs, resulting in more current being induced in the dyno stator windings. These induced currents are dissipated as heat via the braking resistors.

4.2 Temperature Measurement Instrumentation

For the motor temperature measurements, T-type thermocouples are chosen for their robustness and accuracy. Interior temperature measurement points in the motor are strategically chosen to capture the hot spots within the winding. These hot spots are determined by using a FLIR thermal camera to obtain thermograms of the stator winding surface right after shutting down the motor. Example infrared images are shown in Figure 4.2 and it is observed that the hot spots for the motor are located in the slot winding depicted by the red markers. This result aligns with the proposition of [35] which stated that open drip proof machines

dissipate 60% - 80% of heat via the end-shield ports, and the rest through the casing surface of the motor. This means the hottest point in the stator winding will be in the slot winding, not the end-winding.

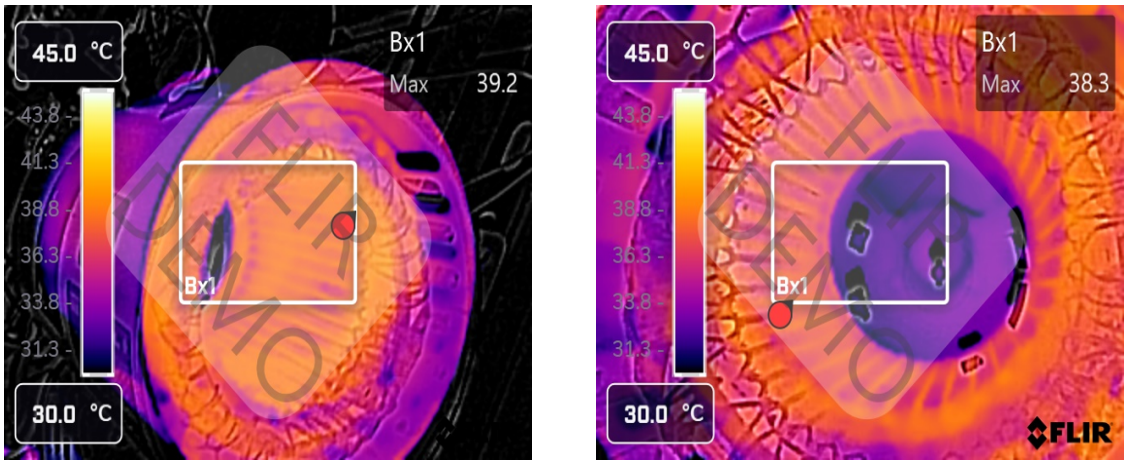

(a) Hot spot 1

(b) Hot spot 2

Figure 4.2: Thermograms showing the hot spots within the stator winding for thermocouple placement

Two mini thermocouple sensors (Omega SCPSS-020U-6) are placed in the slot winding, one on each of the hot spot locations, while two PFA-insulated thermocouple sensors (Omega 5TC-TT-T-24-36) are attached to the end-winding. These four sensors make up the internal thermal measurements for the experiments. Another PFA-insulated thermocouple is attached to the round casing exterior of the induction motor. This sensor captures the casing surface temperature and is useful for the thermal network model calibration. The last set of sensors are the ambient air sensors (three PFA-insulated thermocouples) placed at different distances from the motor casing surface. This is done to evaluate any possible thermal stratification within the controlled environment for the motor and help maintain the average overall ambient temperature around 40°C for all the tests reported here.

4.3 Temperature-Controlled Enclosure for Induction Motor

The maximum ambient temperature for performance tests of induction motors with F-class insulation is $40°$C according to the NEMA standard [36]. A temperature-controlled enclosure is built for the induction motor to make sure the surrounding air is maintained at the standard temperature. This enclosure is made of transparent acrylic sheets with openings on all sides to aid air circulation and mixing with the exterior. The top plate of the enclosure has two (2) thermoelectric systems installed to control the temperature within the box. Each thermoelectric system comprises of four (4) peltier modules, delivering a combined cooling effect of 168 Watts (i.e. a total cooling of 336 W from both systems). A cold plate is attached to the cold end of the modules, while the hot end is thermally connected to a heat sink and fan-cooled. A thermostat controller is connected to each thermoelectric system for accurate temperature regulation. The thermostats have resistance temperature detector (RTD) sensors located as close to the motor as possible which help reduce the thermal stratification within the enclosure and keep the environment within $\pm 5°$C of the standard temperature.

4.4 Thermal Model Parameter Tuning

To calibrate the thermal model, preliminary tests were conducted with the experimental set-up under varying speed and load combinations. The speed settings were diversified into 50%, 75% and 100% speed levels, and the load settings were split into half and full load conditions, making up a test matrix with six combinations listed in Table 4.1. Furthermore, using the collected test results to tune the motor thermal model improves its prediction over a wide range of operating conditions which is the goal of this study.

Motor Speed (%)	Motor Load level	
	Half Load	**Full Load**
50	Test point 1	Test point 2
75	Test point 3	Test point 4
100	Test point 5	Test point 6

Table 4.1: Test matrix for induction motor

The motor thermal model takes two variables as inputs during the parameter tuning phase. These variables include:

- Motor losses, calculated by determining the difference between the input power to the motor and the motor output mechanical power. This overall loss is split into copper and stator core losses by finding the weighted average of each loss component from an electromagnetic transient motor model developed in MATLAB Simscape [37].
- Ambient temperature measured by the thermocouple farthest from the motor within the enclosure.

4.4.1 Test Results

The experimental thermal results collected from the case study motor for each individual test point is analyzed in this section. Figure 4.3 shows the temperature distribution across the motor components for test point 1. The thermal hot spot in the motor is noticed to be the slot winding represented by the magenta trend lines. The maximum slot winding temperature reaches a steady-state value of 76°C after running the motor for 11 hours at 50% speed and half load conditions. The end-winding has the second highest thermal profile according to the plot. The two thermocouples placed on the end-winding record an average temperature of

72°C. Next on the temperature plot is the round frame temperature represented by the green trend line which hits a steady-state value of 59°C. The ambient air temperature reaches the standard ambient temperature of 40°C after 8 hours of test time and is maintained around this value for the rest of the experiment.

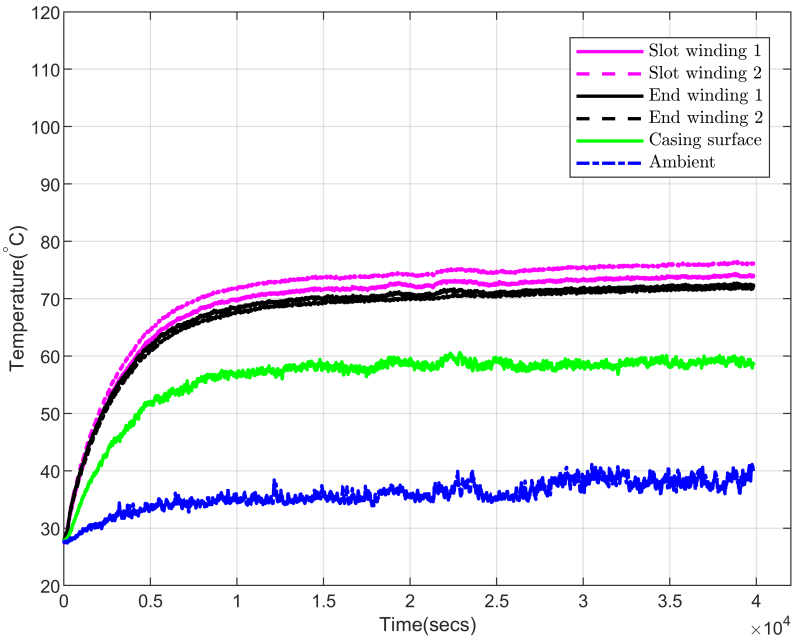

Figure 4.3: Temperature distribution for 50% speed and half load

Temperature distribution for test point 2 is displayed in Figure 4.4 where we immediately notice a higher range of temperature values. The hot spot temperature in this scenario hits a steady-state value of 112°C. This is a 36°C difference from the hot spot value for test point 1 attained by doubling the load on the motor for a similar speed of 50%. Here, the end-winding sensors record temperature values of 105.7°C at steady-state. The round casing of the motor reaches steady-state temperature around 80°C.

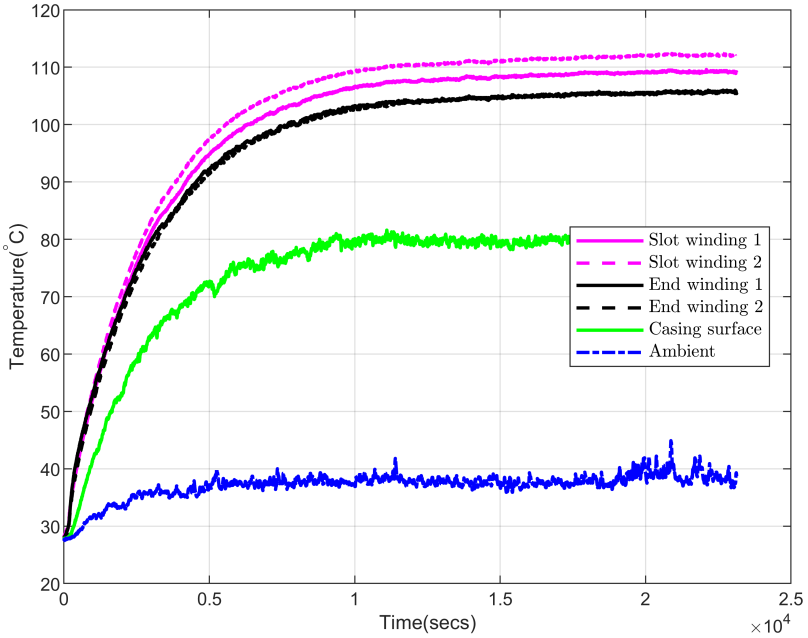

Figure 4.4: Temperature distribution for 50% speed and full load

Test point 3 introduces a higher speed level for the motor and this is seen to impact the temperature distribution in Figure 4.5. Hot spot temperature in this case gets to steady-state at 72°C after 4.7 hours. The end-winding maximum temperature is recorded to be 69°C at steady-state represented by the black trend line. Round frame temperature has a steady-state value of 57°C in this case while the ambient temperature never gets to the standard temperature of 40°C. The ambient temperature hits a maximum of 38°C and plateaus at 36°C.

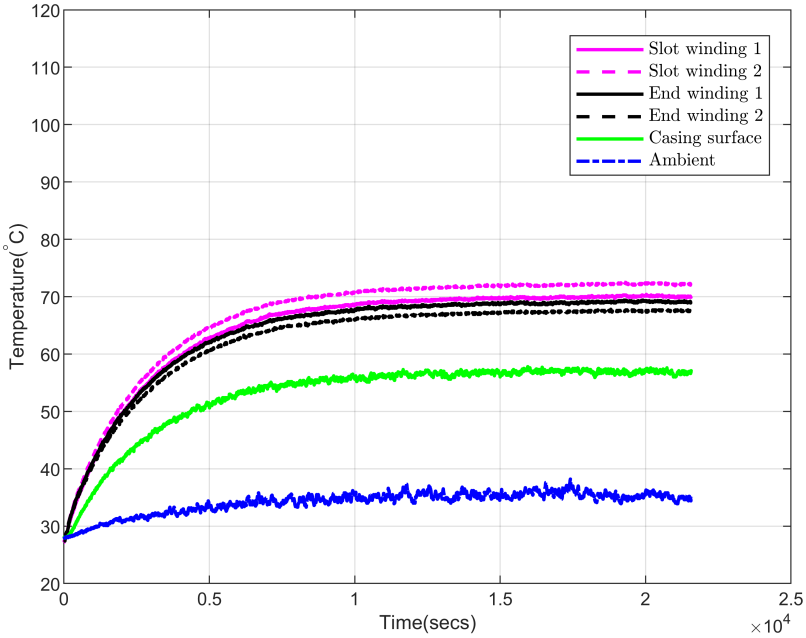

Figure 4.5: Temperature distribution for 75% speed and half load

From Figure 4.6, we can observe an obvious increase in the temperature range recorded for test point 4. The slot winding attains a maximum temperature of 106°C for this case, making a hot spot temperature difference of 6°C from the lower speed test done for the same load level. The end-winding gets to steady-state at a temperature of 101°C and the two thermal sensors record different values in this case. The casing surface records a steady-state temperature value of 78°C. The surrounding air temperature rises to the set level quickly and is controlled by the thermostat for the duration of the test.

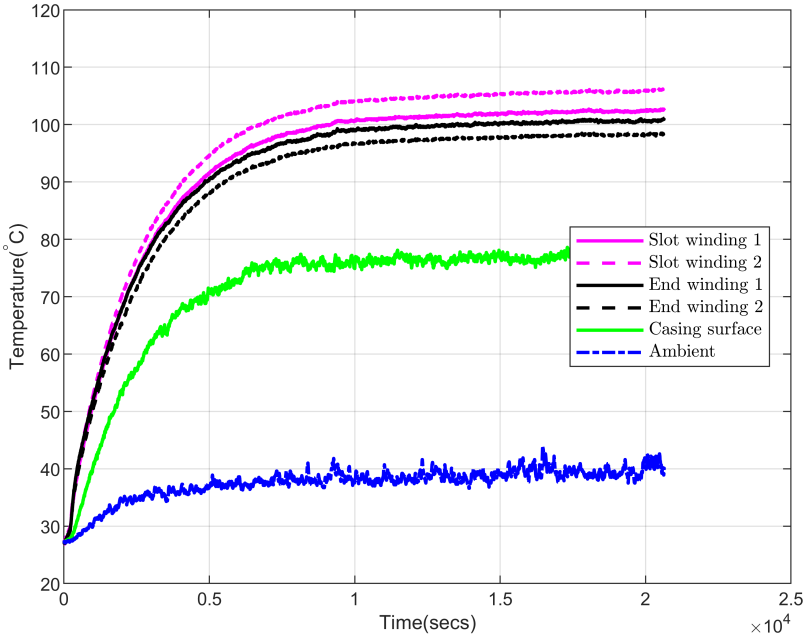

Figure 4.6: Temperature distribution for 75% speed and full load

Maximum speed tests start from test point 5 which is for the 100% speed and half load combination. Figure 4.7 displays the thermal profile for this scenario and we observe the lowest hot spot value recorded for all the tests done in this plot. Slot winding temperature rises to steady-state at 70°C after 8.6 hours. The end-winding records a steady-state temperature of 66.5°C while the round frame shows 56°C at steady-state. Similar to the 75% speed scenario for half load conditions, the ambient temperature for test point 5 does not get to the set level of 40°C.

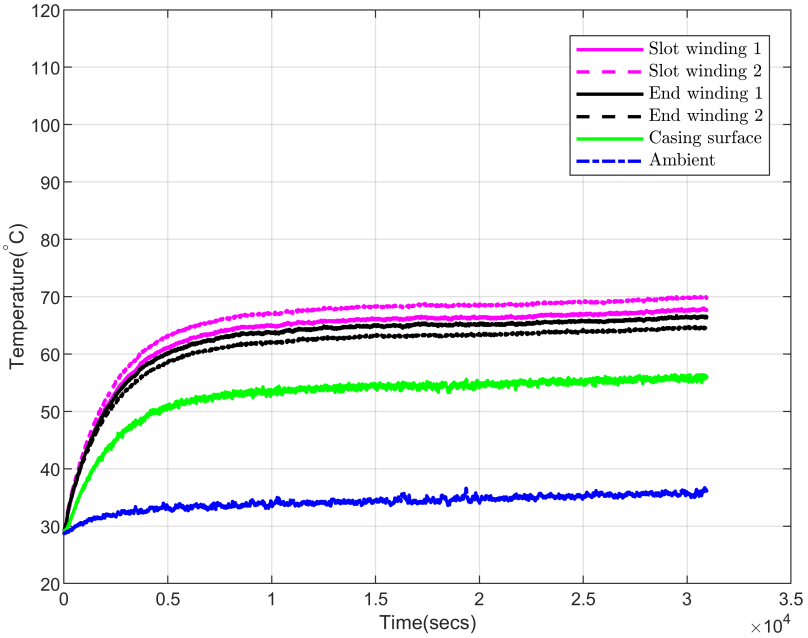

Figure 4.7: Temperature distribution for 100% speed and half load

The final test point represents the most common operational conditions of electric motors where they run at full speed to meet full loads. The temperature distribution for this scenario is shown in Figure 4.8 and the hot spot is seen to reach steady-state at 101.7°C. The end-winding hits steady-state at a temperature of 97°C and the casing surface records a temperature of 74.5°C at steady-state. The surrounding air temperature also rapidly rises to the set level and is maintained by the thermostat.

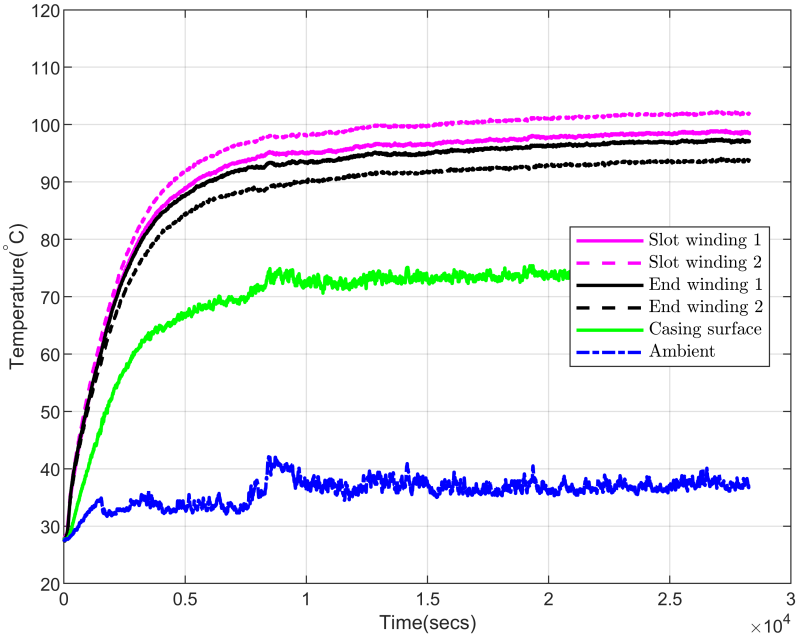

Figure 4.8: Temperature distribution for 100% speed and full load

An overview of the test matrix temperature results show that the worst operational conditions happen during test point 2 where the motor runs at 50% speed and full load where we hit a maximum hot spot temperature of $112°$C. The best case is seen in test point 5 for the 100% speed and half load conditions where we have the lowest slot winding temperature of $70°C$. This is a consequence of the relatively large difference in the rates of heat generation and dissipation for these cases. During test point 2, the motor has fast heat generation but a slow heat dissipation rate. Conversely for test point 5, the motor has slow heat generation but fast heat dissipation. The ambient temperature is maintained within a tolerance of $\pm 5°$C around the set level of $40°$C for all test points.

4.4.2 Individually Tuned Motor Thermal Model Validation Results

The simulation results of the calibrated numerical model are compared with the experimental results and shown from Figure 4.9 to Figure 4.14. The thermophysical parameters in the thermal model are manually fine-tuned to obtain good fits in the temperature profiles for each test case considered. This fine-tuning process generates the best values for the parameters for each test point. As a result, different parameter values are derived for the different test points in this subsection. The transient temperature trend of the simulation results is mainly tied to the thermal capacitances, while the steady-state trend is determined by the thermal resistances. Adjusting these values for each of the test points produce accurate simulation results that track the case study motor test results. Initial and boundary temperature conditions are fed into the numerical model according to the results of the associated laboratory test for each case.

It is necessary to note here that the capacitance parameters, once correctly tuned, must remain constant for all scenarios. The material specific heats do not change for the range of temperature being considered in this study. On the other hand, the steady-state temperatures are largely determined by the convective resistances, which are dependent on the heat transfer coefficient of the components in contact with the surrounding air (the copper end-winding and the motor round casing). As previously stated, the heat transfer coefficient of these components are air velocity-dependent which is confirmed by the fine-tuned parameters, therefore, the resistance parameters, particularly the convective heat transfer coefficients vary from one test point to another. The final values of the specific heat and conductivity that determine the thermal capacitance and resistance for the LPTN model after calibration are tabulated below.

Component	Parameter	
	Specific heat c (J/kgK)	**Conductivity k W/mK**
rotor	460	28
winding	850	292.5
insulation	1500	0.2
stator	1250	22.5
casing	160	58

Table 4.2: Calibrated material parameters for motor thermal capacitance and resistance

Since the calibrated convective heat transfer coefficients are different across the different test points and are a function of the air velocity, mainly, they are shown with their associated motor speed in revolutions per minute (RPM) in Table 4.3. The heat transfer coefficient values for the end-winding fall into the forced convection category as seen on the table. Heat transfer coefficient values for the round frame however are within the natural convection range since the surrounding air around the motor are relatively stationary compared to the former.

It is also important to highlight that due to the geometry and open drip proof enclosure type of the case study electric motor, the heat transfer coefficient of the slot winding is not sensitive to changes in the motor speed. This value is constant as seen previously in Table 3.2 for all the test points considered.

Test Point	Motor Speed (RPM)	Heat Transfer Coefficient (W/m^2K)	
		End-winding	Motor casing
1	870	120	15.5
2	845	123	15.8
3	1320	150	16.5
4	1290	154	17.3
5	1765	222	22
6	1728	193	19.5

Table 4.3: Calibrated heat transfer coefficients for motor components at different speeds

Figure 4.9 overlays the slot winding and round frame temperature results of the simulation model and the laboratory experiment for test point 1. Slot winding 2 temperature (hot spot) is used as the reference for the simulation model winding temperature prediction and we can see a good fit on the plot for the transient and steady-state behaviors. The casing surface also shows good agreement between the test and simulation results.

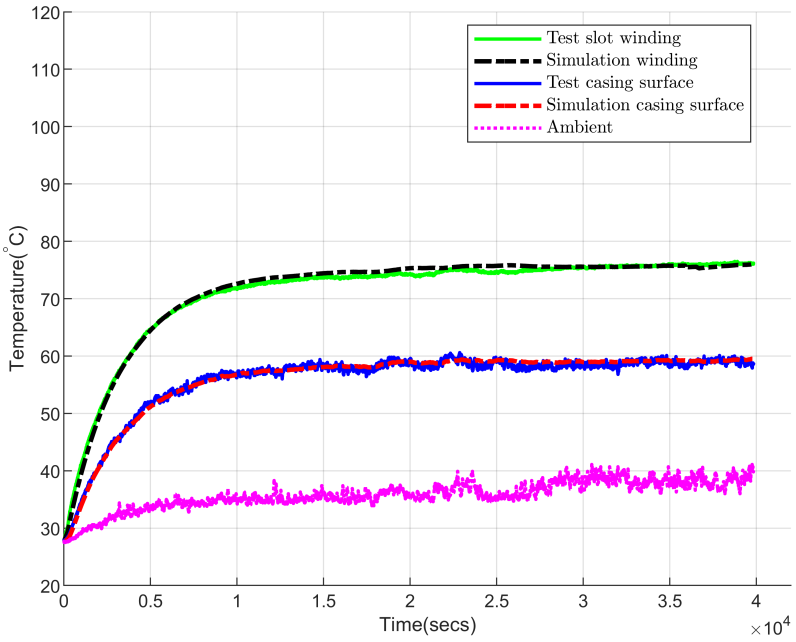

Figure 4.9: Simulation and test thermal profile for 50% speed and half load

The comparison between the tuned thermal model and the test results are displayed in Figure 4.10. The winding temperature of the simulation model follows slot winding 2 temperature with high accuracy after the resistances are readjusted for this case. The casing surface temperature of the LPTN model similarly tracks that of the physical motor with good precision. Since there is an increment in heat generation as a result of the doubled load in this scenario, an increased heat transfer coefficient is expected for the end-winding and round frame.

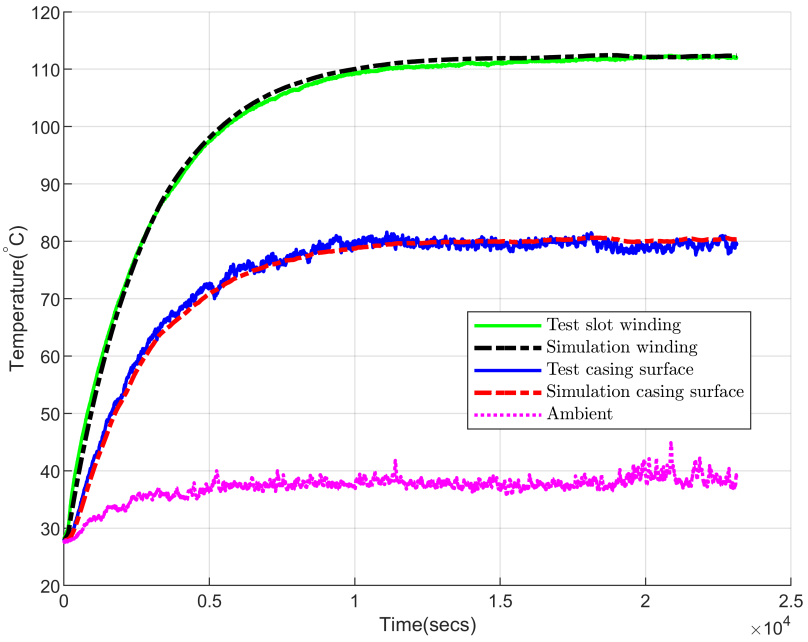

Figure 4.10: Simulation and test thermal profile for 50% speed and full load

Figure 4.11 compares the simulation and experimental thermal profiles of the slot winding and casing surface for test point 3. These temperature values have good agreement with each other for both motor components as seen in the plot. This accuracy is achieved by increasing the heat transfer coefficients of the end-winding and the round frame in the motor thermal model, respectively as shown in Table 4.3, to capture the effect of the new motor speed level for this test point.

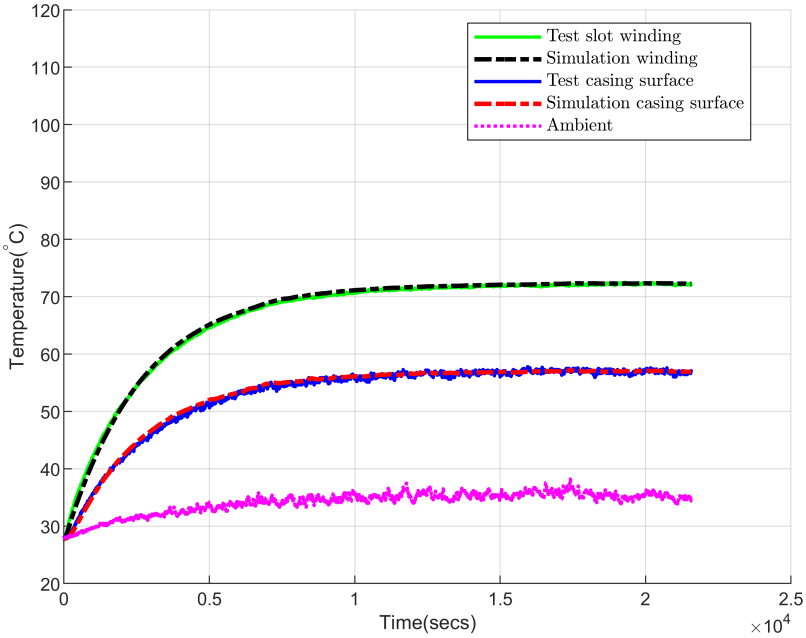

Figure 4.11: Simulation and test thermal profile for 75% speed and half load

During parameter tuning for test point 4, the heat transfer coefficients of the end-winding and round frame are both increased in the numerical model in order to have their thermal profiles track those of the laboratory test. The comparison results are shown in Figure 4.12 and high precision is noticed in the plot for both transient and steady-state phases.

For test point 5 which is the first high speed test, the heat transfer coefficients of the end-winding and casing are increased to their maximum for the test matrix conditions. Since this scenario has the lowest hot spot temperature value recorded, it translates to the simulation model end-winding having the highest heat transfer coefficient. The casing's heat transfer coefficient is also adjusted so that its temperature follows that of the experiment as seen in Figure 4.13.

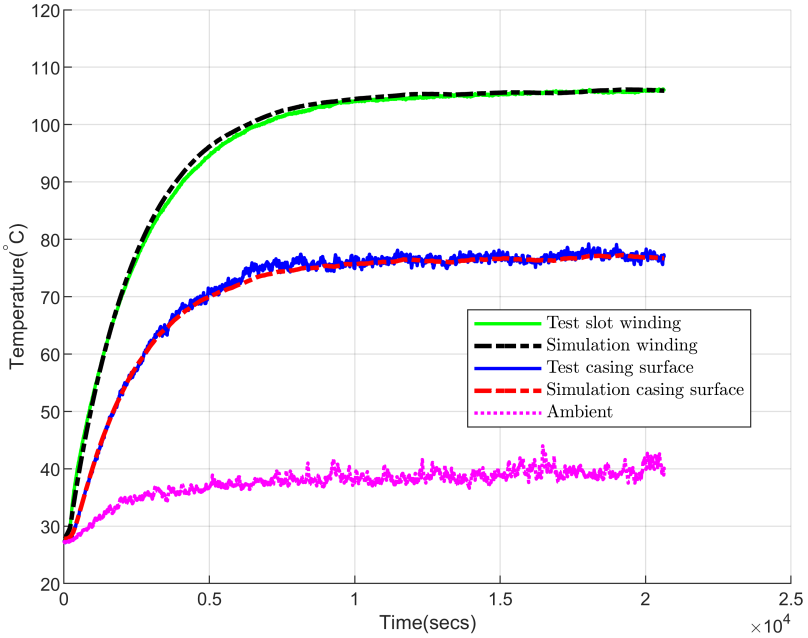

Figure 4.12: Simulation and test thermal profile for 75% speed and full load

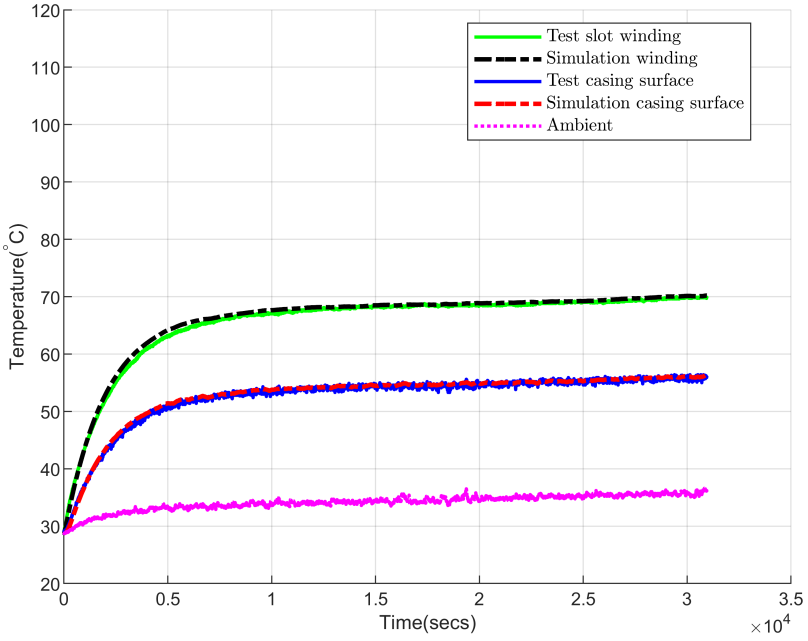

Figure 4.13: Simulation and test thermal profile for 100% speed and half load

Tuning the thermal model parameters for test point 6 gives the results shown in Fig-

ure 4.14. The thermal capacitance is seen to be properly calibrated as the model captures the small bumps in the casing surface at time 2 hours as a result of the ambient air fluctuation. The heat transfer coefficients of the model are decreased in this instance from their previous values in order to accurately predict the experimental thermal profiles of the slot winding and round frame.

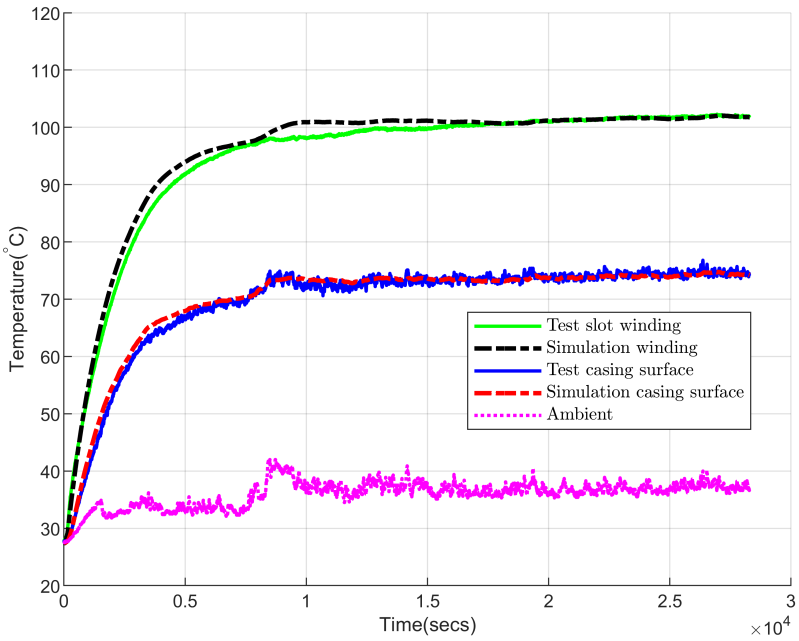

Figure 4.14: Simulation and test thermal profile for 100% speed and full load

4.5 Generic Motor Thermal Model Development

The development of a generic thermal model that accurately predicts the temperature dynamics of an induction motor under dynamic conditions is made possible with a relationship that relates the heat transfer coefficient of the end-winding and the casing surface with the motor speed, respectively. The slot winding heat transfer coefficient is not an influential parameter on the varying thermal dynamics, so it is neglected.

Figure 4.15 shows the correlation between the heat transfer coefficients of the end-

winding and the motor speed at the different test points. The blue trend line representing the correlation is noticed to have a close fit for the 50% and 75% speed levels; however, the deviation increases for the 100% speed test points.

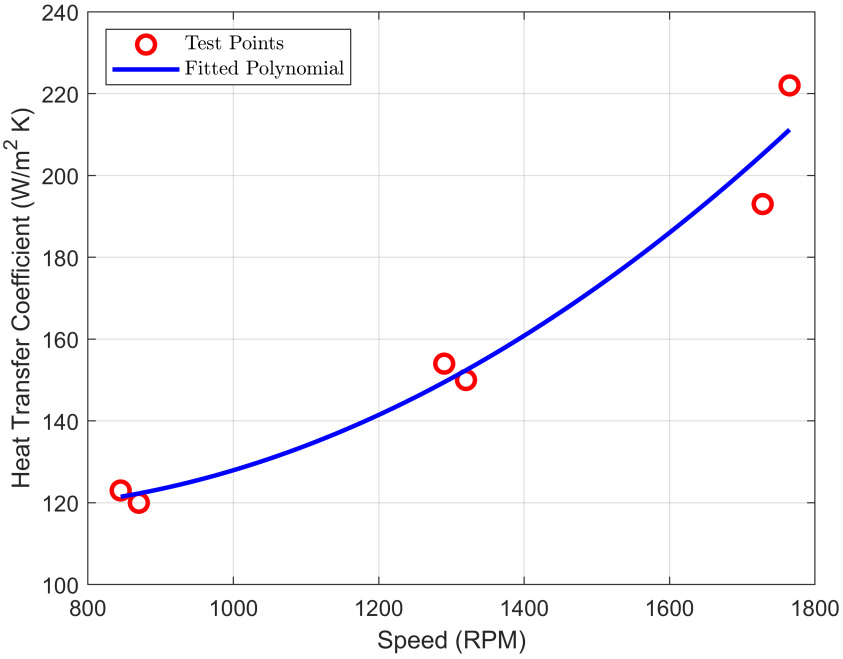

Figure 4.15: Correlation between end-winding heat transfer coefficient and motor speed

This deviation can be attributed to the presence of certain physical phenomena that influence heat transfer coefficient of materials at higher temperatures and air speed which is not captured by the numerical model. These factors can include:

- Airflow patterns that get more complex to simulate with only a lumped parameter network model at higher speeds. Complex airflow patterns inside the motor casing may vary with speed and can be affected by features like air vent locations, or the geometry of cooling fins. These are difficult to model precisely without detailed computational fluid dynamics (CFD) simulations.

- Variations in humidity and air density that may impact convective heat transfer. Higher

humidity or denser air can slightly improve convective cooling, although these effects are subtle and hard to simulate without real-time data.

Figure 4.16 also shows the heat transfer coefficient correlation with the motor speed for the motor round casing in contact with the surrounding air. Similar to the end-winding situation, the deviation of the polynomial fit gradually increases as we move from the 50% speed to the 100% speed levels.

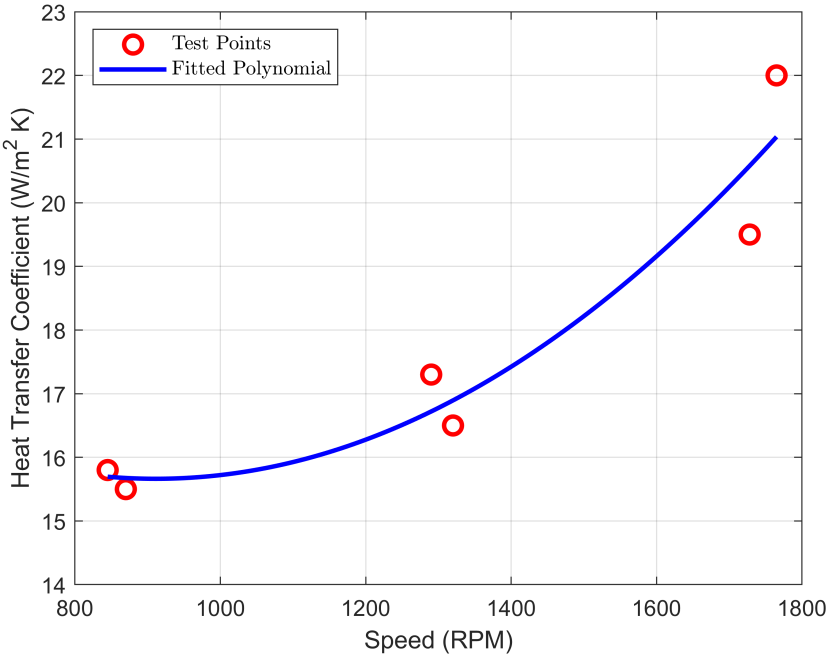

Figure 4.16: Correlation between motor casing heat transfer coefficient and motor speed

Both relationships are a quadratic polynomial fit with the former having a larger output range, given the speed as input. The correlation curve-fit expressions are given below as:

$$h(v)_{end-winding} = 7.28e^{-5}v^2 - 0.0925v + 147.6524, \tag{4.1}$$

$$h(v)_{casing} = 7.37e^{-6}v^2 - 0.0134v + 21.7821 \tag{4.2}$$

Equation 4.1 expresses the dynamic heat transfer parameter for the copper end-winding of

the induction motor, while Equation 4.2 shows the variable heat transfer parameter for the motor round frame. Both these expressions enable the creation of a dynamic motor thermal model that now takes three variables as inputs - losses, ambient temperature, and motor output speed. This dynamic thermal model is a generic model that allows for the prediction of motor component temperatures under different operating conditions.

4.5.1 Generic Motor Thermal Model Tuning Results

The results of the developed generic model are compared with the experimental results and shown from Figure 4.17 to Figure 4.22 in this section. Most of the previously developed thermal simulation models in the literature have been done for fixed rated conditions. These models are not generalizable to varying speed conditions of the electric motor. This section presents the performance of the novel calibrated thermal model built to adapt to varying speed and load conditions.

Figure 4.17 compares the slot winding and round frame temperature results of the generic model and the laboratory experiment for test point 1. Very good accuracy is shown for the temperature distributions considered. The simulation thermal profile for the winding and casing is however lower than those generated by the specifically tuned thermal model for this test point because from Figure 4.15 and Figure 4.16, the heat transfer coefficient is overestimated for the generic model.

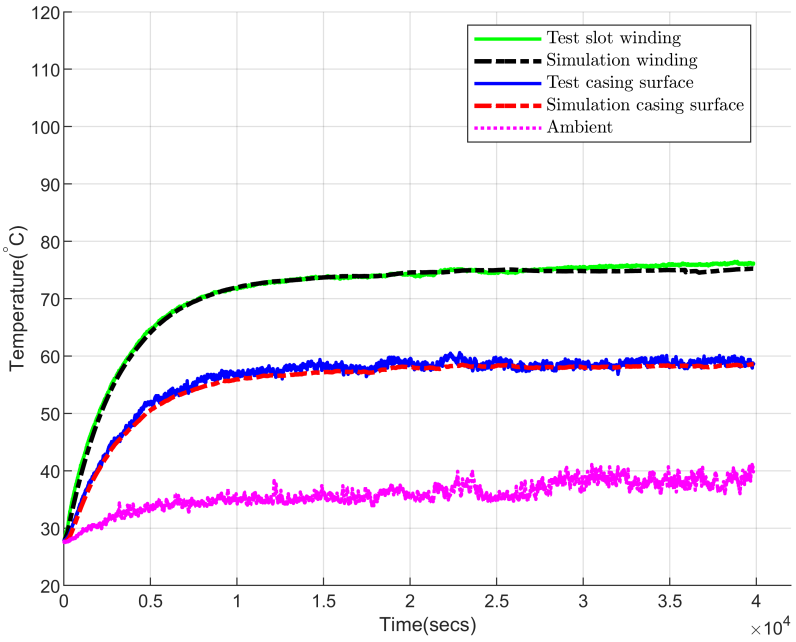

Figure 4.17: Generic model simulation and test thermal profile for 50% speed and half load

For test point 2 results compared in Figure 4.18, the temperature results of the generic model winding accurately tracks slot winding 2 temperature results, however, the casing surface steady-state temperature is overestimated by $1.6°$C in the thermal model. This is consistent with the heat transfer coefficient plot for the motor casing since the quadratic curve underpredicts the heat transfer coefficient and heat loss to the ambient.

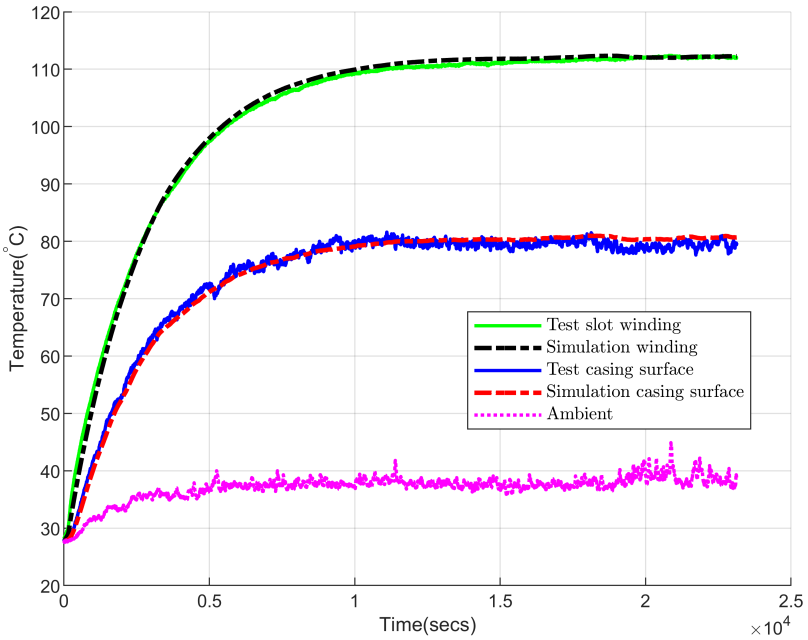

Figure 4.18: Generic model simulation and test thermal profile for 50% speed and full load

Test point 3 simulation results compared with the experimental results in Figure 4.19 show a consistent underestimation of steady-state temperature for the slot winding and round frame. Slot winding 2 temperature and casing surface temperature are underestimated by $1.1°$C and $0.8°$C, respectively, in the generic thermal model. This is consistent with the heat transfer coefficient plots in Figure 4.15 and Figure 4.16 where the polynomial curve overpredicts the heat transfer coefficient in relation to test point 3.

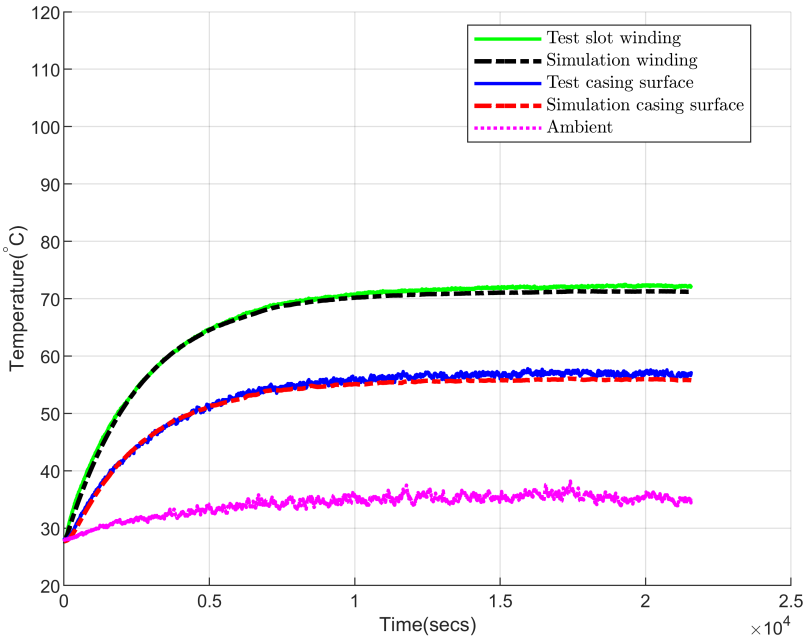

Figure 4.19: Generic model simulation and test thermal profile for 75% speed and half load

Contrastingly, the winding and casing surface temperatures of the simulation model are higher than those of the case study induction motor for test point 4 as noticed in Figure 4.20. The hot spot temperature and round frame temperature are overestimated by $2.3°$C and $1.6°$C, respectively, in the generic thermal model. This is in agreement with the heat transfer coefficient plots where the polynomial curve underpredicts this parameter in the generic thermal model for test point 4.

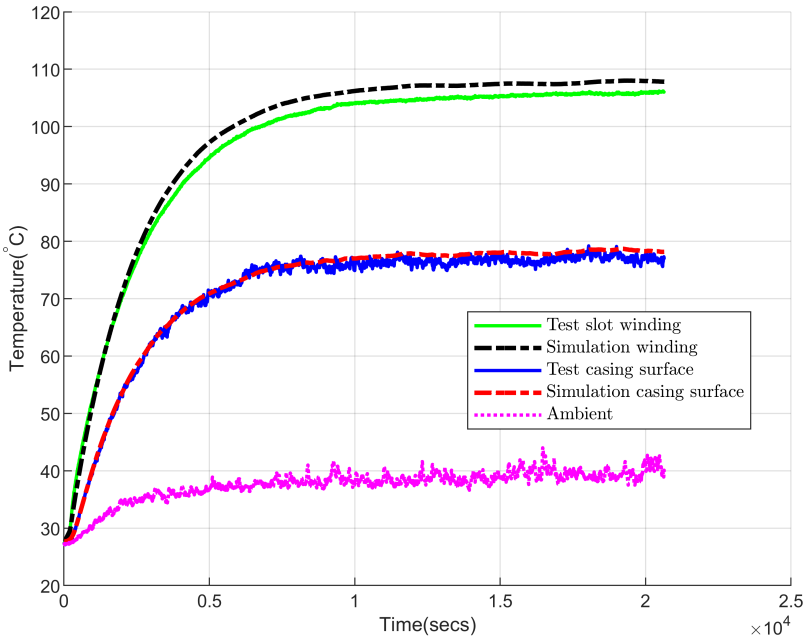

Figure 4.20: Generic model simulation and test thermal profile for 75% speed and full load

For the full speed and half load condition, the steady-state temperatures of the slot winding and round frame are consistently overestimated by the generic thermal model as shown in Figure 4.21. Here, slot winding 2 temperature and casing surface temperature are overestimated by $1.8°$C and $1.3°$C, respectively. This is represented in Figure 4.15 and Figure 4.16 by the quadratic curve underpredicting the heat transfer coefficients for test point 5.

Test point 6 results are compared in Figure 4.22 for the generic model and the test motor. The temperature distribution of the motor components are underestimated by the generic thermal model in this case. The hot spot temperature and the casing surface temperature are underestimated by $3.8°$C and $2.6°$C, respectively. These are the largest prediction gaps calculated for all the test cases considered, and is consistent with the heat transfer coefficient plots where the polynomial curve highly overpredicts the heat transfer coefficient in relation to test point 6.

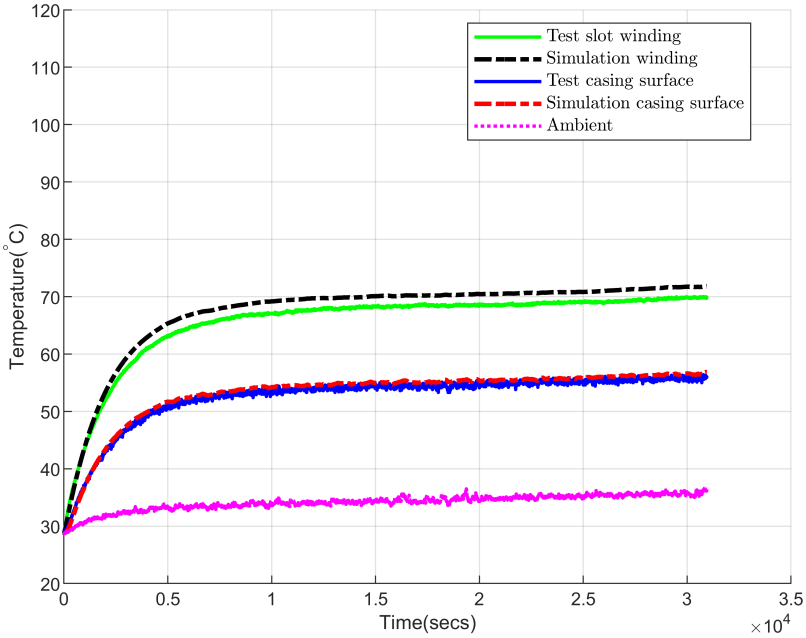

Figure 4.21: Generic model simulation and test thermal profile for 100% speed and half load

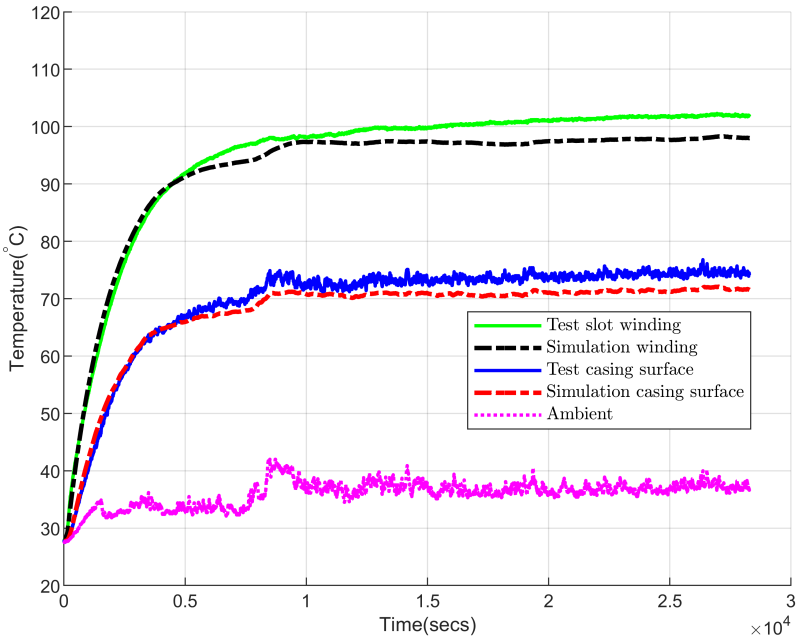

Figure 4.22: Generic model simulation and test thermal profile for 100% speed and full load

Among all the temperature comparison plots, the worst accuracy is seen in Figure 4.22 for

the 100% speed and full load conditions which has the maximum steady-state temperature difference of 3.8°C for the slot winding. The best accuracy is seen in Figure 4.17 for the 50% speed and half load conditions where the simulation results of the generic thermal model tracks the experimental results with very good precision. Generally, the accuracy of the dynamic motor thermal model decreases as we move from test point 1 to test point 6 which is in agreement with the heat transfer coefficient curve fit results shown in the previous section. The motor thermal model has now been fully calibrated and validated with different sets of data. This generic model will be tested with power frequency regulation market data to evaluate its response to flexibility requests in the next chapter.

CHAPTER 5

FREQUENCY REGULATION TEST RESULTS

Real-time power supply and demand balances are critical to ensure stable power frequency and quality power services. However, the growing integration of renewable energy increasingly challenges the power infrastructure due to their uncertain and intermittent nature, and demands more regulation capacity across the power system. Proactive control of variable-speed electric motors in HVAC equipment to accommodate this flexibility need is one of the most cost-effective measures to increase demand flexibility. During provision of frequency regulation services, a power regulation signal is provided by system operations and service providers need to ramp up or down their power use to follow this regulation signal. In this study, we use actual regulation signal retrieved from PJM (Pennsylvania-New Jersey-Maryland Interconnection) database for a random day in August 2024, which has a two-second sampling interval for the entire 24 hours of the day. The regulation signal is normalized to between ± 1.

This chapter evaluates the performance of the case study induction motor by running it under two different testing modes - modulation and baseline test cases. The modulation test involves running the motor under variable speed and load conditions to simulate real-world operating environments where the motor must adapt to changing demands. In contrast, the baseline test imposes constant speed and load conditions, serving as a reference point for assessing the potential aging impact of motor speed modulation. For a legitimate comparison, the overall service provided by the electric motor must be kept the same for both testing scenarios. For motors used in fans, this service is determined by the airflow delivered in

cubic feet over a given time period. Comparing the motor thermal behaviors subject to the same amount of service provision generates insight into the impact of variable operational conditions on motor thermal stresses.

5.1 Motor Performance Curves

This section introduces the conversion process and control strategies employed to translate the raw frequency regulation signal to variable frequency drive (VFD) frequency inputs for the motor and dynamometer. These processes are implemented in the Siemens STEP 7 Professional V17 software package using the ladder logic data and function blocks. Firstly, the raw signal is converted to the induction motor power. The VFD has an operational frequency range of 33% to 100% (i.e. 19.8 Hz to 60 Hz). For safety reasons, the VFD is operated within the 40% to 100% output range for this research work. This translates to a motor output power range of 274.4 W to 1745 W.

Secondly, the scaled power signal is converted to motor speed using the speed-power curve shown in Figure 5.1. The performance curves utilized in this chapter are generated from data collected from an office building air-handling unit (AHU) fan under various operating conditions. Variables recorded include the airflow rate, torque, and power consumption at different fan speed settings. The curve below gives the corresponding speed level for each desired power level, and can be directly converted to a frequency setting for the motor VFD. However, the dynamometer also requires a speed setting for every sample time that leads to the correct load on the induction motor, which will be discussed in next paragraph. The equation relating the motor output power and speed is shown below:

$$power = 0.0004\ speed^2 - 0.0315\ speed + 0.8944 \tag{5.1}$$

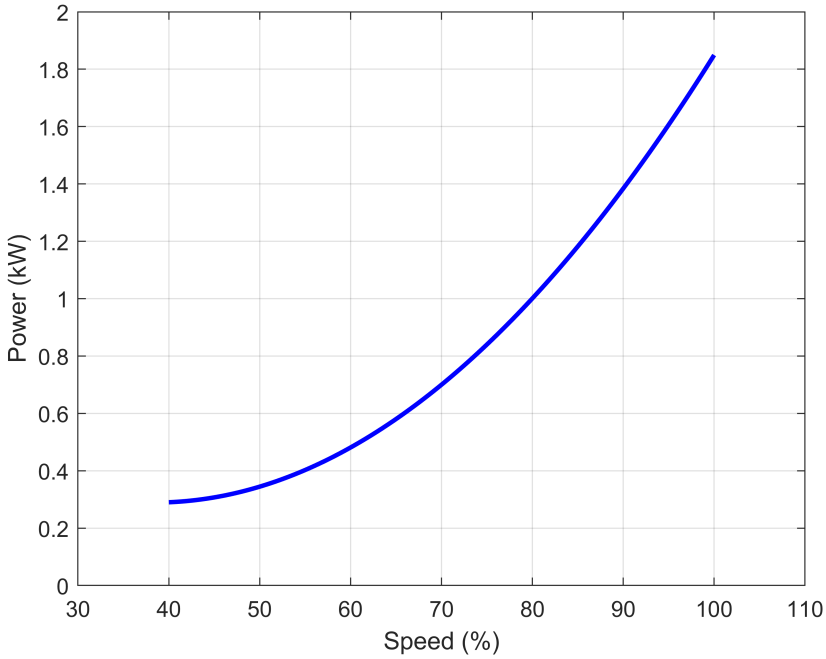

Figure 5.1: Speed vs. Power curve

Next, the motor speed is converted to output torque through the speed-torque curve for the AHU fan displayed in Figure 5.2. The lower speed limit of 40% translates to 3.58 N.m of torque, while the upper speed bound of 100% translates to 10.47 N.m. This plot is seen to be similar to the speed-power curve because motor output torque and output mechanical power are closely related. This speed-torque relationship is expressed in the following equation:

$$torque = 0.0016\ speed^2 - 0.1164\ speed + 5.7987 \tag{5.2}$$

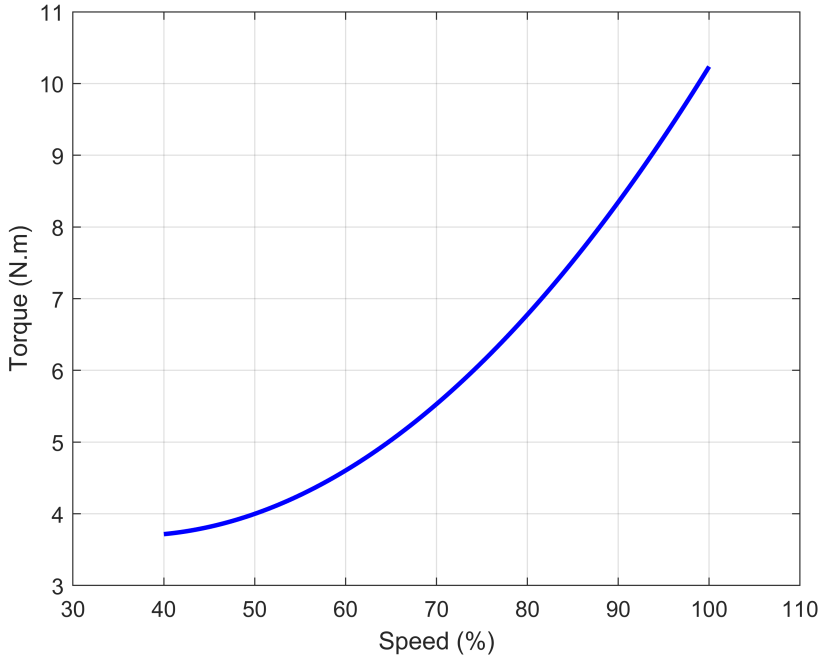

Figure 5.2: Speed vs. Torque curve

Furthermore, the output torque is translated to the required VFD frequency difference between the motor and dynamometer to achieve the required torque. This relationship is determined by conducting series of loading tests at specific speed settings (50%, 60%, 70%, 80%, 90%, and 100%) at the laboratory. The needed frequency difference between the motor and dynamometer VFD to achieve a particular load level is recorded and plotted for the different speed levels. This generates a frequency difference-torque curve for each speed setting. A single performance curve that connects a particular torque value to its commensurate frequency difference across all speed settings is developed. This quadratic curve showing the correlation between the torque and frequency difference over the speed range can be seen in Figure 5.3 with the curve equation being:

$$frequency\ difference = 0.027\ torque^2 - 0.0538\ torque + 0.8313 \tag{5.3}$$

The lower torque limit of 2.75 N.m translates to 0.8 Hz difference on the y-axis, while the

upper torque bound of 10.47 N.m translates to 3.3 Hz difference.

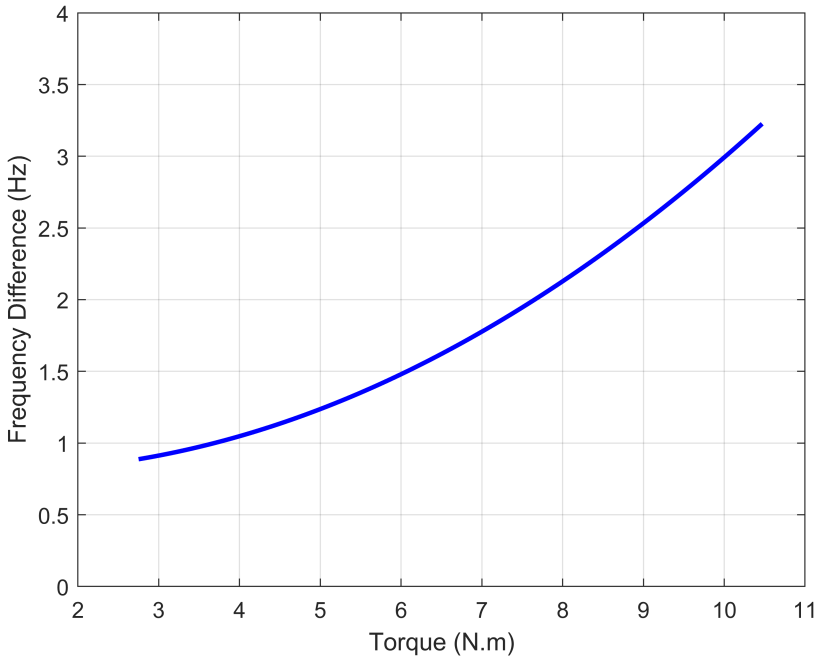

Figure 5.3: Torque vs. Frequency difference curve

Lastly, this frequency difference is subtracted from the associated control frequency input for the induction motor to get the control frequency input for the dynamometer. The frequency regulation signal is now completely processed and the modulation test is ready to be done.

5.2 Modulation Test Results

This section shows the motor test results for the modulation test over 5 hours. The modulation test involves running the motor using a frequency regulation signal as control. Since the frequency regulation signal is energy neutral, power supply must constantly equal demand so the electric grid frequency is maintained within required limits. This means the motor is

run under variable speed and load conditions to replicate real-world operating requirements. Firstly, a warm-up period is required so the motor thermal profile reaches steady-state before the frequency regulation control is turned on. For this study, a warm-up time of 4.3 hours is used to ensure thermal steady state is fully attained for all the motor components. This warm-up is needed to ensure the repeatability of the test and a legitimate comparison with the baseline test results which will be discussed in the next section.

Figure 5.4 shows the alignment of the market power control signal with the actual motor power. The motor output power can be seen to accurately track the input signal during this frequency regulation test with a root mean square error (RMSE) of 36.4 W.

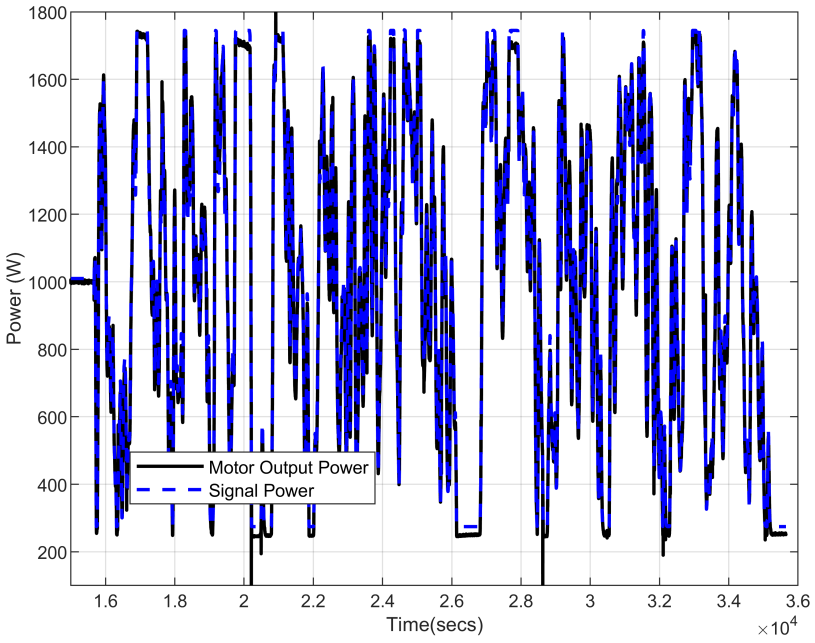

Figure 5.4: Power comparison between signal target and motor result

The motor output torque values are compared with the torque reference signal in Figure 5.5. This variable has a slightly worse accuracy in this comparison largely due to the higher deviation of the torque-frequency difference curve-fit from the actual performance

data points. As a result, we observe a root mean square error (RMSE) of 0.52 N.m in the figure.

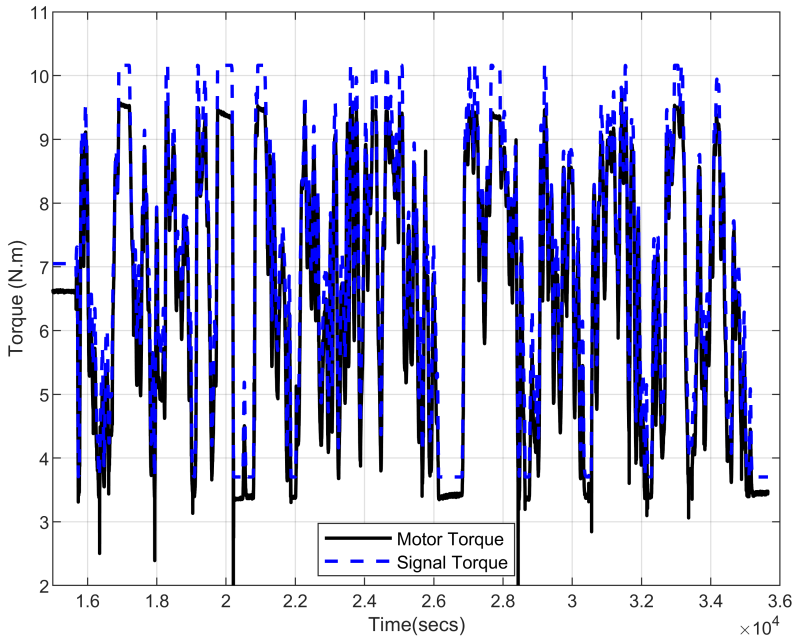

Figure 5.5: Torque comparison between signal target and motor result

Temperature profiles of the motor components for a 10-hour period (warm-up plus testing) are shown in Figure 5.6. The thermal profiles are seen to begin fluctuating after the warm-up period. The initial few hours of the modulation period are used to wash out any transient impact from the initial conditions. The winding temperature reaches a quasi-steady-state of approximately $81°$C, depicted by the dashed red line. The winding temperature rises from a steady-state of $79°$C in the warm-up period to a mean value of $81°$C for the modulation period.

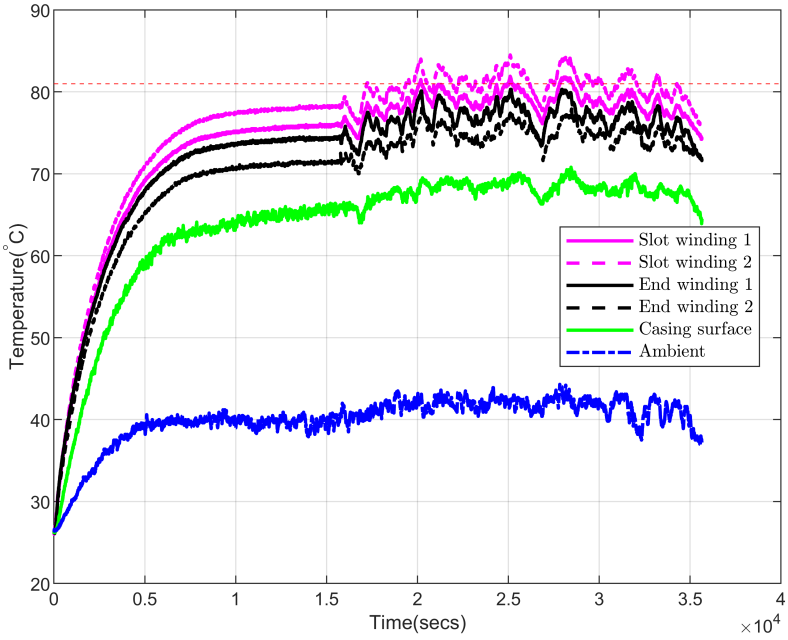

Figure 5.6: Temperature distribution of induction motor for the modulation test

5.3 Baseline Test Results

This section discusses the motor test results for the baseline test over a 5-hour duration, just like the modulation test. Similarly, a warm-up period is required so the motor thermal profile reaches steady-state before starting the baseline test. The baseline test involves running the electric motor at a constant speed and load setting, providing a stable reference point for assessing its operational characteristics. This approach allows for the precise measurement of the motor thermal behavior under steady-state conditions.

To determine the baseline speed setting, the overall service provided by the induction motor during the modulation is required. As previously stated, this service is determined by the airflow (CF) delivered by the motor. The cumulative airflow delivered over the modulation period is calculated and translated to the corresponding motor speed using the speed-airflow

equation and performance curve generated from the office building AHU fan shown in Figure 5.7 below:

$$airflow = -0.023\ speed^2 + 19.588\ speed - 67.861 \tag{5.4}$$

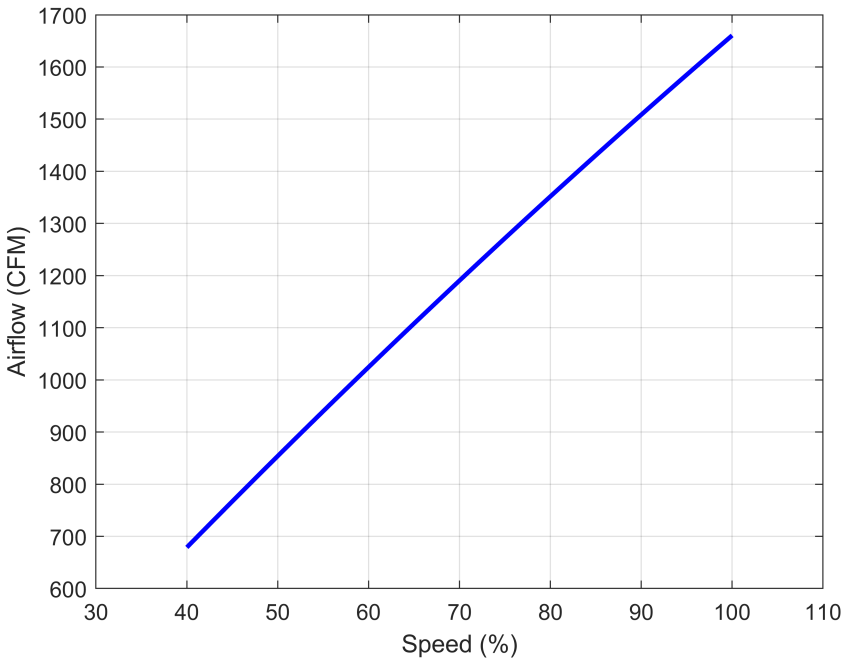

Figure 5.7: Speed vs. Airflow curve

This motor speed is further processed to get the associated frequency difference, and hence, the dynamometer control speed using the processes outlined in section 5.1. The baseline controls assume constant control settings, hence, the motor is simply set to the target conditions after the warm-up period is over.

The temperatures of the motor components are collected over a 10-hour period for consistency with the modulation case and are shown in Figure 5.8. The thermal profiles are seen to decline from the warm-up steady-state level to new steady-state values over the baseline test period. The maximum slot winding temperature is noticed to be approximately $73.7°C$

at final steady-state, depicted by the horizontal dashed line. Hence, the motor slot winding temperature falls from a steady-state of 79°C in the warm-up period to a mean value of 73.7°C over the baseline period.

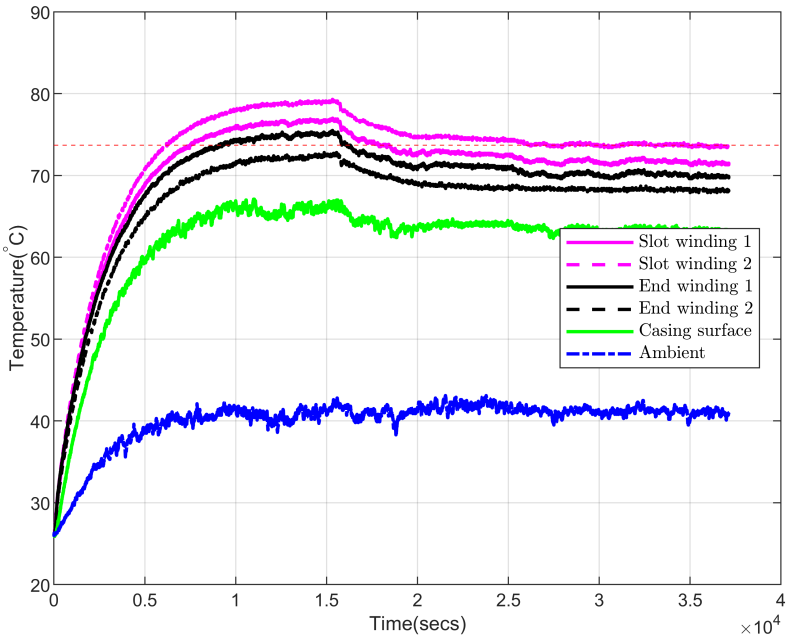

Figure 5.8: Temperature distribution of induction motor for the baseline test

An overall temperature difference of 7.3°C is observed for the motor hot spot between the modulation and baseline scenarios. This signifies an increased thermal stress in the motor parts, and hence, accelerated insulation deterioration when the motor is operated with variable speed control settings for provision of frequency regulation services compared to constant speed control.

5.4 Motor Thermal Model Results

Simulation tests were also conducted using the motor thermal model subject to the modulation and baseline test conditions to determine its accuracy in predicting the temperature

dynamics. The simulation results discussed in this work were generated in approximately 3 seconds of computation time for each test case.

Figure 5.9 compares the simulation results of the motor thermal model with the motor experimental results for the modulation test. The generic thermal model winding temperature has a quasi-steady-state value of approximately $85.8°$C for the modulation operating condition, which is represented by the horizontal dashed line. Relating this averaged value to that observed for the laboratory test, the thermal model overestimates the hot spot temperature by $4.8°$C.

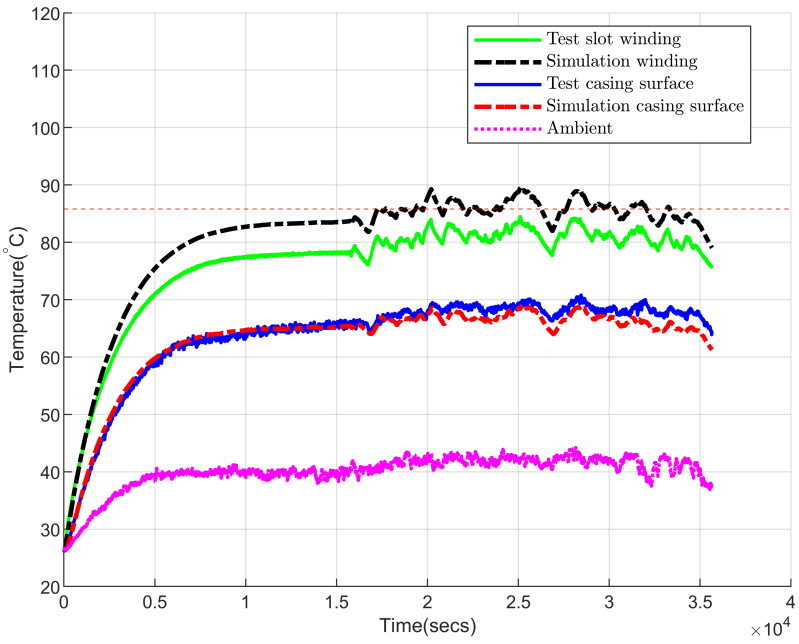

Figure 5.9: Motor simulation and experimental thermal results comparison for the modulation test

For the baseline test, the results of the motor thermal simulation are compared with the experimental results in Figure 5.10. The thermal model winding temperature reaches a baseline steady-state value of $78.3°$C highlighted by the horizontal dashed line. Comparing this

value to the baseline steady-state temperature for the experiment, the thermal model overestimates the hot spot temperature by $4.6°$C.

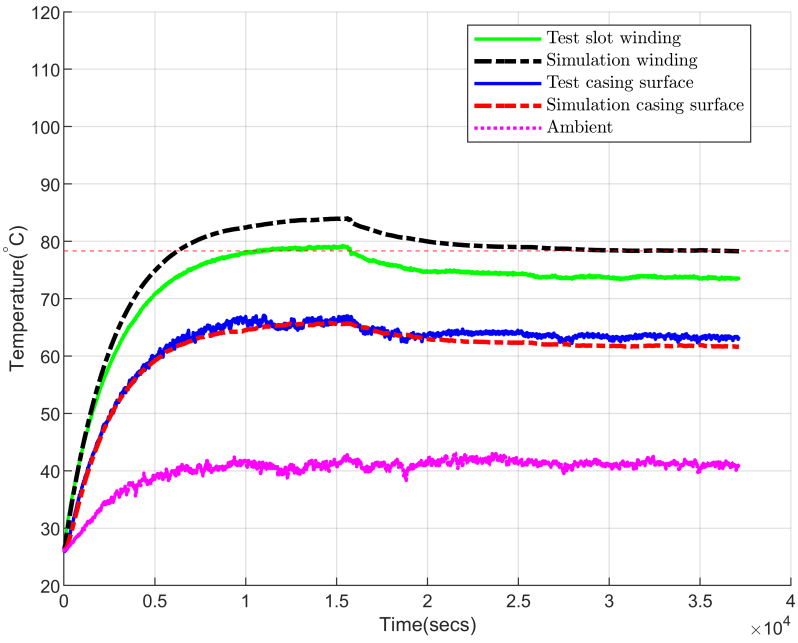

Figure 5.10: Motor simulation and experimental thermal results comparison for the baseline test

The simulation model leads to a temperature difference of $7.5°$C for the copper winding between the modulation and baseline scenarios, a deviation of $0.2°$C from the temperature difference from the laboratory experiments. Although the model overpredicts the steady-state winding temperature by $4.8°$C, it performs well in predicting the copper winding temperature under different dynamic operating conditions and also gives a relatively accurate differential temperature prediction between constant speed and variable speed control for the motor.

CHAPTER 6

CONCLUSIONS

This thesis presented the development of a generic motor thermal model and tested the performance of this model with both step response and frequency regulation tests. The capabilities of the model in predicting the winding temperature were assessed through comparisons to laboratory test results for a case study induction motor under various operational conditions. The results show that the developed numerical model is able to predict the temperature dynamics within the electric motor with a maximum error of $4.8°$C for the slot winding temperature (hot spot) and $2.6°$C for the round casing. This estimation error decreases as the motor speed ramps down from 100% rated speed to 40% speed for all load conditions.

The simulated temperature differential between the constant and modulating speed cases with the thermal model has an error of $0.2°$C, confirming the robustness of the developed thermal model in capturing thermal aging behaviors. Having a high accuracy thermal model like this is essential for determining the aging effect of dynamically loading an induction motor and modulating control of the motor in response to flexibility request over an extended period of time. The resulting insulation degradation due to increased thermal stress can be more readily captured with low computing demand. This enables model-based real-time control of electric motors to minimize lifetime impact.

6.1 Future Work

The current version of the thermal model was calibrated using only six data points, and this limited training data may affect the generalizability of the model. More laboratory tests can

be done to collect diverse operation data and further tune the thermal model parameters in order to reduce the prediction errors and enhance its robustness.

Further work will focus on using this developed model to develop control strategies to mitigate the impact of the flexibility provision on the lifespan of electric motors. However, the model presented in this study is limited to the thermal response only, hence, it needs to be coupled with a fully developed electrical transient motor model for a multi-domain simulation in order to successfully perform full control analysis. The thermal model takes three inputs - losses, motor speed, and ambient temperature - the first two variables are to be outputs from the electrical transient model. This co-simulation process will facilitate design of control and maintenance measures for the electric motor by correlating the predicted hot spot temperature with the loss in useful motor life in years for each operating condition.

REFERENCES

[1] P. Waide and C. U. Brunner, "Energy-efficiency policy opportunities for electric motor-driven systems", 2011.

[2] *Siemens, electromagnetic motors are the world's biggest energy consumers*, https://blogs.sw.siemens.com/en-US/simcenter/electromagnetic-motors-are-the-worlds-biggest-energy-consumers/, Accessed: 2022-04-20.

[3] *Eia, use of energy explained*, https://www.eia.gov/energyexplained/use-of-energy/homes.php, Accessed: 2023-12-18.

[4] *Marketwatch, hvac warranties*, https://www.marketwatch.com/guides/home-warranty/hvac-warranty/, Accessed: 2024-10-02.

[5] S. Khalesidoost, J. Faiz, and E. Mazaheri-Tehrani, "An overview of thermal modelling techniques for permanent magnet machines", *IET Science, Measurement & Technology*, vol. 16, no. 4, pp. 219–241, 2022.

[6] *Eere, variable-speed, low-cost motor for residential hvac systems*, https://www.energy.gov/eere/iedo/variable-speed-low-cost-motor-residential-hvac-systems.

[7] R. Bell, D. McWilliams, P. O'donnell, C. Singh, and S. Wells, "Report of large motor reliability survey of industrial and commercial installations. i", *IEEE Transactions on Industry applications*, vol. 21, no. 4, pp. 853–864, 1985.

[8] O. V. Thorsen and M. Dalva, "Failure identification and analysis for high-voltage induction motors in the petrochemical industry", *IEEE Transactions on Industry Applications*, vol. 35, no. 4, pp. 810–818, 1999.

[9] R. H. Engelmann and W. H. Middendorf, "Handbook of electric motors", *(No Title)*, 1995.

[10] R. De Doncker, A. Vandenput, and W. Geysen, "Thermal models of inverter fed asynchronous machines suited for adaptive temperature compensation of field oriented controllers", in *1986 Annual Meeting Industry Applications Society*, IEEE, 1986, pp. 132–139.

[11] T. W. Dakin, "Electrical insulation deterioration treated as a chemical rate phenomenon", *Transactions of the American Institute of Electrical Engineers*, vol. 67, no. 1, pp. 113–122, 1948.

[12] V. Madonna, P. Giangrande, L. Lusuardi, A. Cavallini, C. Gerada, and M. Galea, "Thermal overload and insulation aging of short duty cycle, aerospace motors", *IEEE Transactions on Industrial Electronics*, vol. 67, no. 4, pp. 2618–2629, 2019.

[13] D. Filusch and H.-G. Herzog, "A new analytical approach for the calculation of the thermal behaviour of an electrical machine", in *2019 IEEE Vehicle Power and Propulsion Conference (VPPC)*, IEEE, 2019, pp. 1–6.

[14] P. Nithiarasu, R. W. Lewis, and K. N. Seetharamu, *Fundamentals of the finite element method for heat and mass transfer*. John Wiley & Sons, 2016.

[15] M. Shanel, S. Pickering, and D. Lampard, "Conjugate heat transfer analysis of a salient pole rotor in an air cooled synchronous generator", in *IEEE International Electric Machines and Drives Conference, 2003. IEMDC'03.*, IEEE, vol. 2, 2003, pp. 737–741.

[16] M. Tosetti, P. Maggiore, A. Cavagnino, and S. Vaschetto, "Conjugate heat transfer analysis of integrated brushless generators for more electric engines", *IEEE Transactions on Industry Applications*, vol. 50, no. 4, pp. 2467–2475, 2014.

[17] A. Boglietti, A. Cavagnino, D. Staton, M. Shanel, M. Mueller, and C. Mejuto, "Evolution and modern approaches for thermal analysis of electrical machines", *IEEE Transactions on industrial electronics*, vol. 56, no. 3, pp. 871–882, 2009.

[18] J. P. Holman, *Heat transfer*, 2020.

[19] G. G. Guemo, P. Chantrenne, and J. Jac, "Parameter identification of a lumped parameter thermal model for a permanent magnet synchronous machine", in *2013 International Electric Machines & Drives Conference*, IEEE, 2013, pp. 1316–1320.

[20] A. J. Grobler, S. R. Holm, and G. van Schoor, "Empirical parameter identification for a hybrid thermal model of a high-speed permanent magnet synchronous machine", *IEEE Transactions on Industrial Electronics*, vol. 65, no. 2, pp. 1616–1625, 2017.

[21] A. Boglietti, M. Cossale, M. Popescu, and D. A. Staton, "Electrical machines thermal model: Advanced calibration techniques", *IEEE Transactions on Industry Applications*, vol. 55, no. 3, pp. 2620–2628, 2019.

[22] F. Liu, J. Hu, Y. Li, and Q. Wang, "Improved thermal model of forced air-cooled motors considering heat transfer in wire-wound winding and end region", *IET Electric Power Applications*, vol. 14, no. 6, pp. 943–950, 2020.

[23] P. S. Ghahfarokhi, A. Kallaste, A. Belahcen, T. Vaimann, and A. Rassõlkin, "Review of thermal analysis of permanent magnet assisted synchronous reluctance machines",

in *2016 Electric Power Quality and Supply Reliability (PQ)*, IEEE, 2016, pp. 219–224.

[24] O. Wallscheid and J. Bocker, "Design and empirical identification of a lumped parameter thermal network for permanent magnet synchronous motors with physically motivated constraints", in *2015 IEEE International Electric Machines & Drives Conference (IEMDC)*, IEEE, 2015, pp. 1380–1386.

[25] O. Wallscheid and J. Böcker, "Global identification of a low-order lumped-parameter thermal network for permanent magnet synchronous motors", *IEEE Transactions on Energy Conversion*, vol. 31, no. 1, pp. 354–365, 2015.

[26] M. Lovera, M. Bergamasco, and F. Casella, *Robust control and linear parameter varying approaches, vol. 437 of lecture notes in control and information sciences*, 2013.

[27] E. G. Gedlu, O. Wallscheid, and J. Böcker, "Permanent magnet synchronous machine temperature estimation using low-order lumped-parameter thermal network with extended iron loss model", in *The 10th international conference on power electronics, machines and drives (PEMD 2020)*, IET, vol. 2020, 2020, pp. 937–942.

[28] G. Verez, H. Tiegna, G. Barakat, and G. Hoblos, "Analytical thermal modelling of axial flux permanent magnet synchronous machines", in *2012 XXth International Conference on Electrical Machines*, IEEE, 2012, pp. 2799–2805.

[29] V. Madonna, P. Giangrande, and M. Galea, "Influence of insulation thermal aging on the temperature assessment in electrical machines", *IEEE Transactions on Energy Conversion*, vol. 36, no. 1, pp. 456–467, 2020.

[30] A. H. Mohamed, A. Hemeida, A. Rashekh, H. Vansompel, A. Arkkio, and P. Sergeant, "A 3d dynamic lumped parameter thermal network of air-cooled yasa axial flux permanent magnet synchronous machine", *Energies*, vol. 11, no. 4, p. 774, 2018.

[31] A. H. Mohamed, A. Hemeida, H. Vansompel, and P. Sergeant, "Parametric studies for combined convective and conductive heat transfer for yasa axial flux permanent magnet synchronous machines", *Energies*, vol. 11, no. 11, p. 2983, 2018.

[32] L. Roggio, *Reduction of a detailed thermal model lumped parameters approach for an osv induction motor*, 2019.

[33] H. Liu, J. A. Luta, S. D. Pekarek, and J. A. Weibel, "Electromagnetic-thermal co-optimization to minimize case-to-winding temperature rise in permanent magnet machines", *Applied Thermal Engineering*, vol. 238, p. 122 132, 2024.

[34] O. Badran, H. Sarhan, and B. Alomour, "Thermal performance analysis of induction motor", *International Journal of Heat and Technology*, vol. 30, no. 1, pp. 75–88, 2012.

[35] J. P. G. De Abreu and A. E. Emanuel, “Induction motor thermal aging caused by voltage distortion and imbalance: Loss of useful life and its estimated cost”, in *2001 IEEE Industrial and Commercial Power Systems Technical Conference. Conference Record (Cat. No. 01CH37226)*, IEEE, 2001, pp. 105–114.

[36] “Ansi/nema mg 1-2021 Motors and Generators”, American National Standards Institute, Standard, Jun. 2022.

[37] P. Krause, “Analysis of electric machinery and drive systems”, *IEEE Press google schola*, vol. 2, pp. 203–210, 2002.